Plasticity in oligomerization, operator architecture, and DNA binding in the mode of action of a bacterial B_{12}-based photoreceptor

Jesús Fernández-Zapata[‡1], Ricardo Pérez-Castaño[§1], Juan Aranda[¶‖], Francesco Colizzi[¶‖], María Carmen Polanco[§], Modesto Orozco[¶‖**], ⓘ S. Padmanabhan[‡2], and Montserrat Elías-Arnanz[§3]

From the [‡]Instituto de Química Física "Rocasolano," Consejo Superior de Investigaciones Científicas, 28006 Madrid, the [§]Departamento de Genética y Microbiología, Área de Genética (Unidad Asociada al Instituto de Química Física "Rocasolano," Consejo Superior de Investigaciones Científicas), Facultad de Biología, Universidad de Murcia, Murcia 30100, the [¶]Institute for Research in Biomedicine (IRB Barcelona), The Barcelona Institute of Science and Technology, Barcelona, the [‖]Joint BSC-IRB Research Program in Computational Biology, Baldiri Reixac 10–12, 08028 Barcelona, and the [**]Department of Biochemistry and Biomedicine, University of Barcelona, 08028 Barcelona, Spain

Edited by Ruma Banerjee

Newly discovered bacterial photoreceptors called CarH sense light by using 5'-deoxyadenosylcobalamin (AdoCbl). They repress their own expression and that of genes for carotenoid synthesis by binding in the dark to operator DNA as AdoCbl-bound tetramers, whose light-induced disassembly relieves repression. High-resolution structures of *Thermus thermophilus* $CarH_{Tt}$ have provided snapshots of the dark and light states and have revealed a unique DNA-binding mode whereby only three of four DNA-binding domains contact an operator comprising three tandem direct repeats. To gain further insights into CarH photoreceptors and employing biochemical, spectroscopic, mutational, and computational analyses, here we investigated $CarH_{Bm}$ from *Bacillus megaterium*. We found that apo-$CarH_{Bm}$, unlike monomeric apo$CarH_{Tt}$, is an oligomeric molten globule that forms DNA-binding tetramers in the dark only upon AdoCbl binding, which requires a conserved W-X_9-EH motif. Light relieved DNA binding by disrupting $CarH_{Bm}$ tetramers to dimers, rather than to monomers as with $CarH_{Tt}$. $CarH_{Bm}$ operators resembled that of $CarH_{Tt}$, but were larger by one repeat and overlapped with the −35 or −10 promoter elements. This design persisted in a six-repeat, multipartite operator we discovered upstream of a gene encoding an Spx global redox-response regulator whose photoregulated expression links photooxidative and general redox responses in *B. megaterium*. Interestingly, $CarH_{Bm}$ recognized the smaller $CarH_{Tt}$ operator, revealing an adaptability possibly related to the linker bridging the DNA- and AdoCbl-binding domains. Our findings highlight a remarkable plasticity in the mode of action of B_{12}-based CarH photoreceptors, important for their biological functions and development as optogenetic tools.

Light is a crucial environmental factor that directly or indirectly signals diverse biological processes but can also cause damage of cellular components such as proteins, lipids, and DNA (1–6). To detect and respond to light, living organisms employ photoreceptor proteins, which are classified into distinct families based on their associated light-sensing chromophore (5, 7). A newly discovered and widespread family of bacterial photoreceptors uses as its chromophore one of the two biologically relevant forms of vitamin B_{12}, 5'-deoxyadenosylcobalamin (AdoCbl).[4] In AdoCbl a 5'-deoxyadenosyl (5'-dAdo) group is covalently bound through its 5'-carbon to the cobalt atom in the B_{12} corrin ring, as the upper axial ligand. The prototype of this family, CarH, is a transcription factor that regulates light-dependent expression, typically of its own gene and of those for the synthesis of carotenoids (8–13), which quench singlet oxygen and other reactive oxygen species to mitigate photooxidative damage (2, 6). The discovery of CarH unveiled a novel biological facet of vitamin B_{12}, that as the light-sensor of a photoreceptor (9, 11, 12), and enlarged the toolkit for optogenetics and related applications (14–17).

Details on the molecular mechanism of action of CarH photoreceptors emerged from studies of $CarH_{Mx}$ and $CarH_{Tt}$ from the Gram-negative bacteria *Myxococcus xanthus* and *Thermus thermophilus*, respectively (8–13, 18). Essentially, AdoCbl and light regulate the oligomeric state of CarH and its cooperative operator DNA-binding and repressor activity to directly control transcription (8, 11). In the dark, binding of AdoCbl to

[4] The abbreviations used are: AdoCbl, 5'-deoxyadenosylcobalamin; 5'-dAdo, 5'-deoxyadenosyl; ANS, 8-anilinonaphthalene-1-sulfonate; DBD, DNA binding domain; Cbl, cobalamin; CTT, casitone-Tris; DR, direct repeat; EMSA, electrophoretic mobility shift assay; GdmCl, guanidinium chloride; MeCbl, methylcobalamin; Km, kanamycin; MD, molecular dynamics; RNAP, RNA polymerase; SEC, size-exclusion chromatography; bis-Tris, 2-[bis(2-hydroxyethyl)amino]-2-(hydroxymethyl)propane-1,3-diol; TSS, transcription start site; qRT, quantitative reverse transcription.

apoCarH, a monomer, leads to the formation of a tetramer, whose binding to its operator represses transcription; light (*blue*, *green*, UV) provokes photolysis of the AdoCbl Co-C bond and release of the 5′-dAdo group, causing tetramer disassembly to monomers and loss of operator binding, thus allowing transcription (Fig. S1*A*). Crystal structures of the free and DNA-bound CarH$_{Tt}$ tetramer in the dark and the light-exposed monomer together with corroborative mutational and DNA-binding analyses, have provided atomic level insights into its architecture and mode of action (9). An autonomously folded ~75-residue N-terminal winged-helix DNA-binding domain (DBD), of the type found in bacterial MerR family proteins, is connected by a flexible linker to an also autonomous, ~210-residue C-terminal light-sensing oligomerization domain (Fig. S1*B*). The latter structurally mirrors the classical methionine synthase methylcobalamin (MeCbl)-binding module (19), consisting of a four-helix bundle and a Rossmann-fold domain, but is repurposed to bind AdoCbl, whose 5′-dAdo upper axial ligand is bulkier than the methyl group in MeCbl. Two AdoCbl-bound C-terminal domains pack as head-to-tail dimers, and two such dimers assemble as the dark-state tetramer, in which the four DBDs are splayed around the surface (Fig. S1*C*) (9). The consequence is a unique DNA-binding mode wherein the CarH$_{Tt}$ tetramer uses three of its four MerR-type DBDs to contact three contiguous 11-bp (bp) direct repeats (DRs), one of which overlaps the −35 promoter element recognized by RNA polymerase (RNAP) holoenzyme with the primary σ factor σ^A (9). By contrast, typical MerR proteins are usually homodimers that use their DBDs to recognize operators with inverted DNA repeats (20–23). The inactive light-state monomer retains the overall dark CarH$_{Tt}$ protomer structure. However, a large shift of its four-helix bundle subdomain (which caps the 5′-dAdo moiety of AdoCbl) relative to the Rossmann-fold provokes tetramer disassembly and loss of DNA binding (9). Intriguingly, the photochemistry underlying Co-C photolysis of CarH$_{Tt}$-bound AdoCbl, whose molecular basis remains elusive, differs from that known for this cofactor, free or enzyme-bound, and allows safe use of AdoCbl (by preventing release of its 5′-dAdo group as a radical) in light-dependent gene regulation (10, 24).

Whether this unusual AdoCbl- and light-dependent oligomerization, DNA binding, and photochemistry apply to other CarH homologs must be addressed for a broader understanding of the action and evolution of this new photoreceptor family. It is also relevant to their expanding use in optogenetics and other applications (14–16). Here, we report our analysis of the homolog from the Gram-positive bacterium *Bacillus megaterium* that we denote as CarH$_{Bm}$ (Fig. S1*D*). It reveals several new insights on CarH photoreceptors, and significantly clarifies and extends previous data (25). We show that unlike the well-folded AdoCbl-bound forms, apoCarH$_{Bm}$ is a molten globule oligomer that does not bind operator DNA, and that its AdoCbl-driven transition to a DNA-binding tetramer depends crucially on a W-X_9-EH motif. CarH$_{Bm}$ operators overlap with the −35 or −10 promoter regions and have the same design as the CarH$_{Tt}$ operator, but are larger by one DR. Even so, CarH$_{Bm}$ binds to the CarH$_{Tt}$ operator *in vitro*. This DNA-binding flexibility may stem from the DNA- and AdoCbl-binding domains being

bridged by a longer linker in CarH$_{Bm}$. We also identified a multipartite six-repeat operator upstream of a new CarH$_{Bm}$-regulated gene encoding an Spx family transcription regulator, typically involved in oxidative stress responses in the phylum Firmicutes (26, 27). Altogether, our findings indicate a plasticity, within otherwise conserved modes of AdoCbl binding, oligomerization, operator design, and DNA binding, which underlies the action of a B$_{12}$-based CarH photoreceptor in light-dependent gene expression.

Results

CarH$_{Bm}$ conserves crucial CarH$_{Tt}$ DNA- and AdoCbl-binding motifs

CarH$_{Bm}$ regulates light-induced carotenoid synthesis to produce a colony color change from white to pale yellow in *B. megaterium* strain QM B1551 (25). This also occurs with strain DSM 32 (Fig. 1*A*) whose CarH$_{Bm}$, examined in this study, is 99% identical in sequence to that in strain QM B1551 (Fig. S2*A*). Consistent with its role as a repressor of carotenoid synthesis, deleting *carH$_{Bm}$* in strain DSM 32 resulted in a strong yellow colony color in the dark or light (Fig. 1*A*). CarH$_{Bm}$ and CarH$_{Tt}$ have similar predicted secondary structures (Fig. S2*B*), which coincide well with the CarH$_{Tt}$ crystal structure (Fig. S1, *B–D*). Sequence alignment (Fig. S1*D*) indicates that CarH$_{Bm}$ retains: (*a*) almost every residue of the conserved R-X-WE-X-RY-X_6-R-X_5-R-X-Y motif (X: any amino acid) in the DBD involved in contacts with operator DNA in the structure of the CarH$_{Tt}$-DNA complex, hinting at a shared mode of DNA recognition; (*b*) the W-X_9-EH-$X_{32−39}$-E-X-H-XX-G-X_{41}-S-X-T/V-$X_{(22−30)}$-GG signature found in the C-terminal domain of putative AdoCbl-binding light-sensing modules (12). In CarH$_{Tt}$, the W-X_9-EH motif caps the AdoCbl 5′-dAdo group and is crucial for binding to AdoCbl (9). The E-X-H-XX-G-X_{41}-S-X-V-$X_{(22−30)}$-GG corresponds to the canonical B$_{12}$-binding motif first reported for MeCbl-dependent methionine synthase (19), where the conserved His replaces the dimethylbenzimidazole base as the lower axial cobalt ligand, in the so-called base off/His-on B$_{12}$ binding mode (9). The presence of the AdoCbl-binding light-sensing signature in CarH$_{Bm}$ suggests a similar role (CarA$_{Mx}$, a homolog that oligomerizes and acts independently of B$_{12}$, lacks the Trp and four adjacent C-terminal residues; Fig. S1*D*) (11, 13). CarH$_{Tt}$ C-terminal residues Arg-176 and Asp-201 are crucial for head-to-tail dimer formation, and Gly-160 and Gly-192 for tetramer assembly (9). Of these, CarH$_{Bm}$ conserves only Gly-192 as Gly-205 (Fig. S1*D*), suggesting that despite conserved secondary structures, DNA- and AdoCbl-binding motifs, CarH$_{Bm}$ and CarH$_{Tt}$ may differ in dimer and tetramer assembly.

CarH$_{Bm}$ oligomerization, UV-visible absorbance, and DNA-binding

We assessed CarH$_{Bm}$ oligomerization and its binding to specific cobalamins using size-exclusion chromatography (SEC). ApoCarH$_{Bm}$ eluted with an apparent molecular mass of ~109 kDa (Fig. 1*B*), compared with the 36.3-kDa monomer value calculated from sequence or determined by MS. With AdoCbl present, CarH$_{Bm}$ eluted in the dark with a molecular mass of ~138 kDa, corresponding to a tetramer, and when exposed to
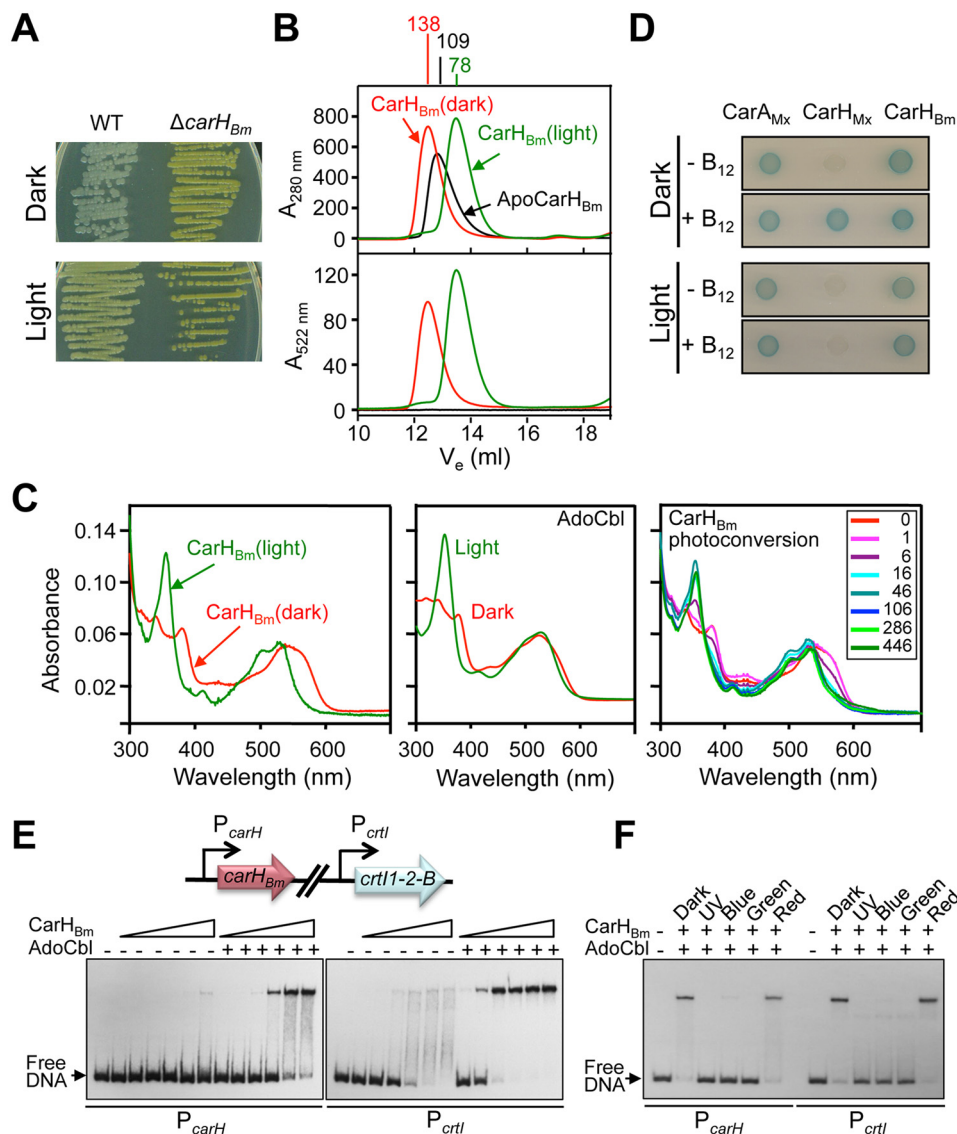
Figure 1. Effects of B$_{12}$ and light on CarH$_{Bm}$ oligomerization and DNA binding. *A*, colony color of *B. megaterium* strain DSM 32 and its *carH$_{Bm}$*-deleted derivative grown in the dark and light. *B*, SEC profiles (off a Superdex200 analytical column) of CarH$_{Bm}$ in the apo form or with AdoCbl present in the dark or after 5-min exposure to green light. Apparent molecular masses are indicated in kDa at the *top*. *C*, UV-visible absorbance spectra of the eluted AdoCbl-bound CarH$_{Bm}$ peak (*left panel*) and free AdoCbl (*middle panel*) in the dark or after 5-min exposure to green light, and photoconversion of the CarH$_{Bm}$ peak (*right panel*) eluted in the dark on stepwise illumination with green light for the times (s) indicated. *D*, two-hybrid analysis in *E. coli* with cells expressing T25 and T18 fusions of CarH$_{Bm}$ and, as controls, CarH$_{Mx}$ or CarA$_{Mx}$, spotted on plates containing X-Gal in the dark or exposed to light in the presence or absence of vitamin B$_{12}$, as indicated. *Blue color* of the spot indicates interaction. *E*, representative EMSA gel for CarH$_{Bm}$ binding to 170-bp DNA probes corresponding to the P*$_{carH}$* and P*$_{crtI}$* promoter regions (scheme on top) in the dark at increasing CarH$_{Bm}$ concentrations (12.5, 25, 50, 100, 200, and 400 nM), with or without a 5-fold molar excess of AdoCbl present, as indicated. *F*, representative EMSA gel of the effects of UV (360 nm), *blue* (405 nm), *green* (520 nm), and *red* (660 nm) light on CarH$_{Bm}$ binding to probes P*$_{carH}$* and P*$_{crtI}$*. Samples with P*$_{carH}$* or P*$_{crtI}$* and 400 or 50 nM CarH$_{Bm}$, respectively, plus 5-fold molar excess of AdoCbl, were incubated in the dark for 30 min and then irradiated for 5 min with the indicated light prior to EMSA.

light with molecular mass of ~78 kDa, expected for a dimer; and both forms absorbed at 522 nm, in addition to 280 nm, consistent with bound cobalamin (Cbl) (Fig. 1*B*). Protein and AdoCbl estimates in the eluted peaks indicated 1:1 stoichiometry. Our SEC data for AdoCbl-CarH$_{Bm}$ (hereafter CarH$_{Bm}$, for simplicity) mirror those in an earlier report (25). However, we found that the UV-visible absorbance spectrum of CarH$_{Bm}$ in the dark was distinct from that obtained upon light exposure (Fig. 1*C*, *left panel*), and not the same as reported previously (25). Moreover, the UV-visible spectra for CarH$_{Bm}$ in the dark and light resembled, respectively, those known for intact AdoCbl and for its photolyzed form, free (Fig. 1*C*, *middle panel*)

or bound to CarH$_{Tt}$ (9–11). In addition, photoconversion of CarH$_{Bm}$ from the dark to the light state was clearly apparent in the UV-visible spectral changes recorded upon stepwise illumination (Fig. 1*C*, *right panel*), with isosbestic points coincident with those reported for CarH$_{Tt}$ photoconversion (10). The previous study (25) reported analytical ultracentrifugation data for dark-state CarH$_{Bm}$ that indicated a substantial presence of a species whose sedimentation coefficient coincided with that for the light-exposed state. We therefore conclude that inadvertent photolysis of dark-state samples must account for the anomalous data reported in that study (25). Finally, we used bacterial two-hybrid analysis to check CarH$_{Bm}$ oligomerization *in vivo*.

Consistent with the SEC data, $CarH_{Bm}$ self-interacted *in vivo* independently of light or B_{12} (like $CarA_{Mx}$), unlike $CarH_{Mx}$ (Fig. 1D) or $CarH_{Tt}$ (11).

Electrophoretic mobility shift assays (EMSA) using two 170-bp DNA probes, P_{carH} and P_{crtI}, for the two promoter regions containing the proposed $CarH_{Bm}$ operators (25), indicated that $CarH_{Bm}$ binds to both probes in the dark to yield a defined retarded band (Fig. 1E). On the other hand, apoCarH$_{Bm}$ binds poorly, the diffuse smear with P_{crtI} at the higher protein concentrations hinting weak unstable binding. The data suggest higher affinity for the P_{crtI} probe, because ~5-fold less protein was required to produce a retarded band of comparable intensity to that using P_{carH}. DNA binding was abolished in samples with $CarH_{Bm}$ upon irradiation with near-UV, blue or green (but not red) light (Fig. 1F), indicating that the dimer formed in the light cannot bind DNA. (ApoCarH$_{Bm}$ binds to MeCbl to form dimers in the dark that do not bind DNA, and remain as dimers in the light (Fig. S3).)

Thus, our data correct the previously reported anomalous UV-visible absorbance for the dark-state $CarH_{Bm}$, and confirm that AdoCbl is specifically required to transition, in the dark, from an apoCarH$_{Bm}$ oligomer that does not bind DNA to a DNA-binding tetramer, which is disrupted by light to a dimer unable to bind DNA. Moreover, our data suggest a higher affinity of $CarH_{Bm}$ for its operator at P_{crtI} than for that at P_{carH}.

ApoCarH$_{Bm}$ is a molten globule

Structural differences may explain why apoCarH$_{Bm}$ does not bind DNA, despite an oligomeric state close to that of the AdoCbl-bound tetramer. We therefore compared the apo and the dark and light $CarH_{Bm}$ forms using circular dichroism (CD) and fluorescence spectroscopy. Far-UV CD spectra, with minima at 208 and 222 nm, indicated significant helical secondary structure for all three $CarH_{Bm}$ forms (28). The mean molar residue ellipticity at 222 nm ($[\theta]_{222}$ in deg cm^2 dmol^{-1}), which correlates with helix content (29), was $-15,300$ (~42% helix) for dark- or light-exposed $CarH_{Bm}$ and somewhat lower ($-11,600$, ~33% helix) for apoCarH$_{Bm}$ (Fig. 2A). Near-UV CD spectra were similar for dark- and light-exposed $CarH_{Bm}$, with fine structures typical of native proteins with well-packed aromatic side chains, but were less well-defined and intense for the apo form suggesting that it is loosely packed (Fig. 2B) (30). $CarH_{Bm}$, with five Trp, yielded an intrinsic fluorescence emission maximum of (337 ± 2) nm in the apo and in both holo forms (Fig. 2C) that red-shifted to 356 nm for the denatured form in 6 M guanidinium chloride (GdmCl), with <20% drop in intensity relative to the holo forms. This indicates that the tryptophans are shielded from solvent in all three native forms (28).

Metal or cofactor-free apoproteins often are molten globules, which are highly dynamic states with native-like secondary structure and a loosely packed, solvent-accessible protein core (30). Consequently, molten globules can interact with the indicator dye ANS (8-anilinonaphthalene-1-sulfonate) and produce a marked blue shift and enhancement in its fluorescence, low in aqueous solutions or in the presence of native proteins (31, 32). Dark- or light-exposed $CarH_{Bm}$ blue-shifted the ANS fluorescence emission maximum from 527 to 482 and 489 nm, respectively, but with little enhancement in intensity
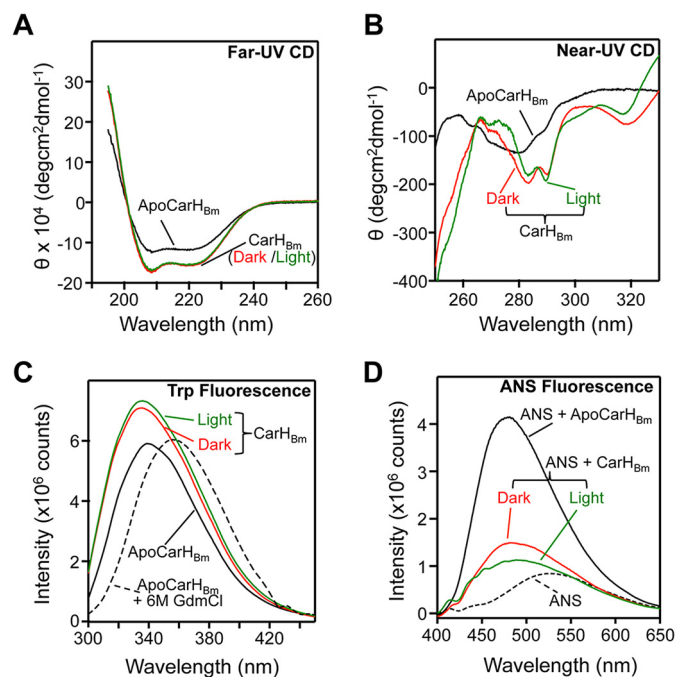
Figure 2. CD and fluorescence spectroscopy of CarH$_{Bm}$. *A*, far-UV CD spectra of 3–4 μM apoCarH$_{Bm}$ (*black*), or CarH$_{Bm}$ in the dark (*red*) or light-exposed (*green*). The same color code is used in *B–D*. *B*, near-UV CD spectra of apoCarH$_{Bm}$ (16 μM), and dark or light-exposed CarH$_{Bm}$ (27 μM). *C*, intrinsic Trp fluorescence emission spectra (excitation at 290 nm) of 2 μM apoCarH$_{Bm}$, dark- or light-exposed CarH$_{Bm}$, and apoCarH$_{Bm}$ in 6 M GdmCl. *D*, ANS fluorescence emission spectra (400–650 nm, excitation at 370 nm) of 20 μM ANS alone, and in the presence of 2 μM apoCarH$_{Bm}$ or CarH$_{Bm}$ (dark- or light-exposed).

(<30%; Fig. 2D). By contrast, apoCarH$_{Bm}$ blue-shifted the ANS fluorescence emission to 481 nm and enhanced its intensity significantly (~500%), consistent with apoCarH$_{Bm}$ being a molten globule (Fig. 2D). In comparison, apoCarH$_{Tt}$, a monomer whose high-resolution structure is unknown, exhibited <60% ANS fluorescence enhancement relative to free ANS or to the dark or light holo forms (Fig. S4D), despite the otherwise analogous spectral (and hence, related structural) characteristics of $CarH_{Tt}$ and $CarH_{Bm}$ (Fig. S4, A–C). ApoCarH$_{Bm}$ is thus an oligomeric molten globule, with a loosely folded structure distinct from that of the AdoCbl-bound form, which may explain its inability to bind operator DNA.

CarH$_{Bm}$ requires its W-X₉-EH motif for AdoCbl-binding, oligomerization, DNA-binding, and repressor activity in vivo

The 5'-dAdo group in dark-state $CarH_{Tt}$ is in close proximity to the Trp, Glu, and His (Fig. 3A) (9) of a W-X_9-EH motif that is highly conserved in CarH homologs, as mentioned earlier (12). The Trp side chain contacts one side of the 5'-dAdo ribose, which also forms a hydrogen bond with the Glu, and the His is involved in contacts at the dimer interface; and AdoCbl-binding, tetramer formation, and DNA-binding by $CarH_{Tt}$ were impaired when the Trp or Glu was mutated to Ala, and abolished for such a mutation of the His (9). Thus far, mutational analysis of the W-X_9-EH motif has been performed only with $CarH_{Tt}$, whose oligomerization varies from that of $CarH_{Bm}$. We therefore tested the effects *in vitro* and *in vivo* of mutating in the $CarH_{Bm}$ motif (Fig. S1D) Trp-143, Glu-153, and His-154 to Ala, and Glu-153 to Asp (a conservative change that has not been
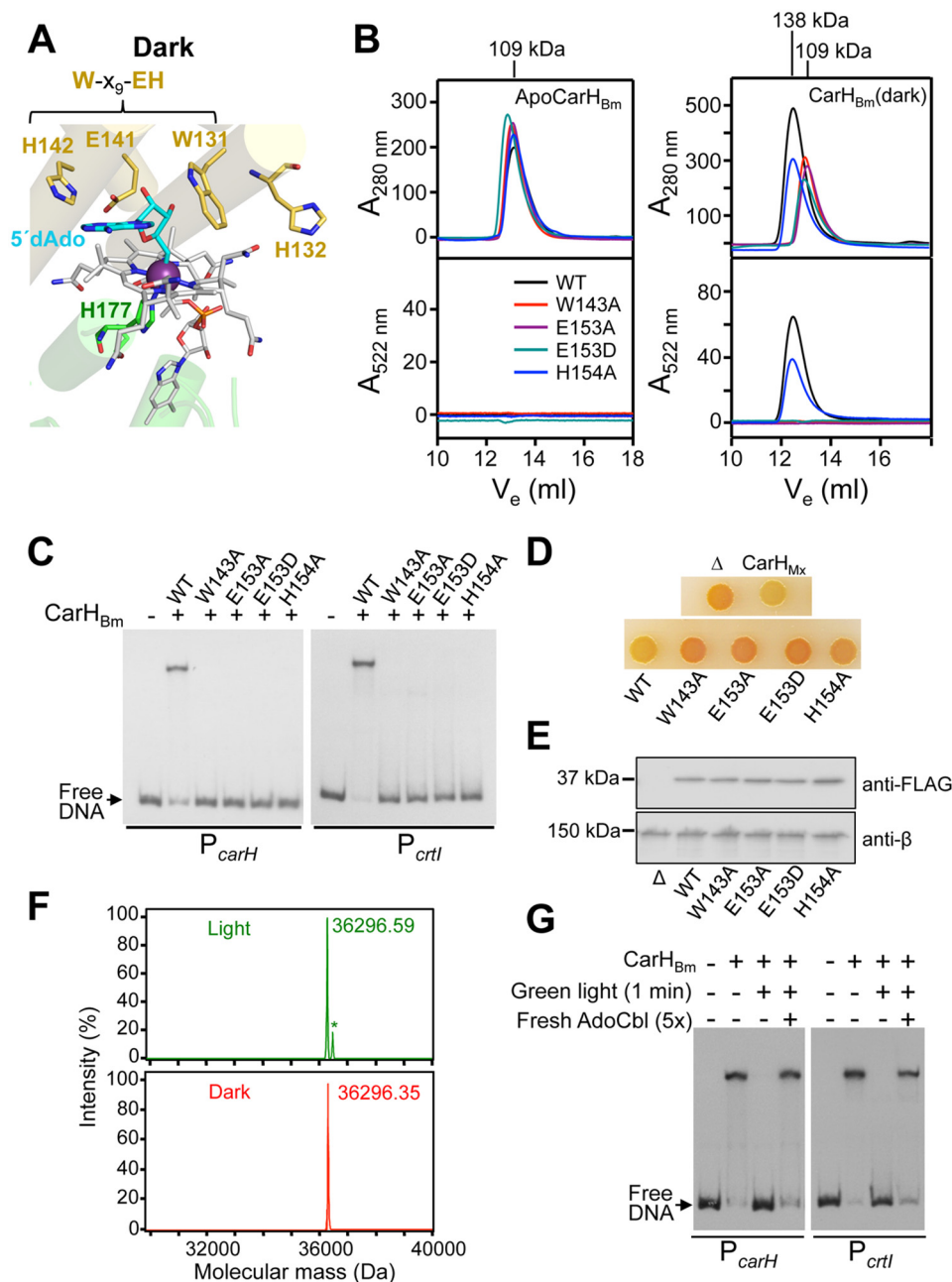
Figure 3. Dependence of AdoCbl binding, oligomerization, DNA-binding and function on the conserved W-X$_9$-EH motif in CarH$_{Bm}$. *A*, close-up of the B$_{12}$-binding site in the dark-state CarH$_{Tt}$ showing Trp-131, Glu-141, and His-142 of the W-X$_9$-EH motif surrounding the 5′-dAdo group (*cyan*) of AdoCbl (*gray* with *cobalt as a dark violet sphere*), the lower axial His-177 cobalt ligand, and His-132, which shifts with the helix bundle in light-exposed CarH$_{Tt}$ to provide the upper axial cobalt ligand. *B*, SEC elution traces for WT (*WT*), and the W143A, E153A, E153D, and H154A CarH$_{Bm}$ mutants in the apo (*left panels*) and the dark AdoCbl-bound forms (*right panels*). Elution was tracked using absorbance at 280 (*top panels*) and 522 nm for cobalamin (*bottom panels*), with molecular masses of the peaks shown on the *top* and curve color code in the *bottom left panel*. *C*, representative EMSA for the binding of native CarH$_{Bm}$ (WT) and its mutants (100 nM protein with 5-fold molar excess of AdoCbl) to 170-bp P$_{carH}$ and P$_{crtI}$ probes in the dark. *D*, color phenotype of *M. xanthus* MR2648 strain without (negative control, "Δ") or with the gene encoding CBm (WT), its W143A, E153A, E153D, or H154A variants, or CarH$_{Mx}$ (positive control) with an N-terminal FLAG tag under the control of a vanillate-inducible promoter. CTT-agar plates containing AdoCbl (1 μM) and vanillate (20 μM) were spotted with 10 μl of cells (grown in the dark to A$_{550}$ = 0.7) and then incubated at 33 °C for 2 days in the dark. *E*, Western blotting of cell extracts of *M. xanthus* expressing WT and its variants (grown in the dark to A$_{550}$ = 0.7 in CTT with 1 μM AdoCbl and 20 μM vanillate) probed with anti-FLAG antibodies (*top*) or, as loading control, anti-RNAP β antibodies (*bottom*). *F*, ESI-TOF mass spectra of CarH$_{Bm}$ in the dark (*bottom*) and after exposure to *green light* (*top*). The same molecular mass for both forms indicates that a tightly bound Cbl adduct is not formed in the light, in contrast to CarH$_{Tt}$ (9). The *small peak with an asterisk* is an unidentified impurity. *G*, EMSA showing that DNA binding is restored, after exposure of CarH$_{Bm}$ (400 nM) to *green light*, by adding fresh AdoCbl in the dark.

analyzed in CarH$_{Tt}$). Far-UV CD spectra for the mutant proteins were similar to that for the WT whether or not AdoCbl was present, indicating that the mutations did not significantly affect CarH$_{Bm}$ secondary structure (Fig. S5A). All four mutant proteins were molten globules in the apo form, like the WT

protein, with blue-shifted and strongly enhanced ANS fluorescence (Fig. S5B). However, the presence of AdoCbl diminished ANS fluorescence only for the H154A mutant, suggesting that this mutant, but not the others, can transition from a molten globule to a fully folded form. Data from SEC were consistent.

In the apo form, all four mutants eluted like the WT protein (Fig. 3B, *left panels*). Upon incubation with AdoCbl in the dark, the W143A, E153A, and E153D mutants continued to elute like the apo forms (molecular mass of ~109 kDa), the lack of absorbance at 522 nm revealing negligible binding to AdoCbl; by contrast, the H154A mutant eluted as an AdoCbl-bound tetramer with molecular mass of ~138 kDa, like WT CarH$_{Bm}$ (Fig. 3B, *right panels*). Nonetheless, the H154A mutant was found to have a lower affinity for AdoCbl (K_D ~850 nM) than the WT protein (K_D ~210 nM, comparable with ~250 nM for CarH$_{Tt}$) (10), as estimated from UV-visible absorbance titrations (Fig. S5C). Thus, AdoCbl binding was most affected by the Trp or Glu mutations in CarH$_{Bm}$, but by the His mutation in CarH$_{Tt}$ (9), which may be related to apoCarH$_{Bm}$ being a molten globule oligomer and apoCarH$_{Tt}$ a monomer. Interestingly, the conservative E153D mutation also strongly impaired AdoCbl binding and transition to the proper tetramer fold, suggesting a strict requirement for Glu in the W-X_9-EH motif.

In EMSA with P$_{carH}$ and P$_{crtI}$, the characteristic retarded band produced in the dark and presence of AdoCbl by WT CarH$_{Bm}$ was not observed with its W143A, E153A, or E153D mutants (Fig. 3C), consistent with these mutations impeding AdoCbl binding. The H154A mutant was also impaired in DNA binding, in line with its lower affinity for AdoCbl (Fig. 3C); and the mutants continued to bind to DNA poorly relative to WT even at higher proteins concentrations (Fig. S5D). These data therefore support the finding that AdoCbl-induced transition to the proper tetramer fold is necessary for DNA binding, and that this depends on the W-X_9-EH motif. Because diminished operator binding by the mutants would reduce repressor activity, we analyzed the effects of the mutations on the regulatory action of CarH$_{Bm}$ *in vivo* by performing complementation tests in *M. xanthus*, a heterologous host previously used for studies with CarH$_{Tt}$ (11). The recipient strain employed (MR2648) exhibits an orange color in the dark (Fig. 3D) as a result of constitutive carotenoid synthesis, due to the lack of CarH$_{Mx}$ and CarA$_{Mx}$ (the B$_{12}$-independent repressor of carotenogenesis). To allow control of AdoCbl supply, MR2648 also lacks PduO, the adenosyltransferase required to produce intracellular AdoCbl in *M. xanthus* (11). We generated MR2648-derived strains (Table S1) that express, under the control of the vanillate-inducible P$_{van}$ promoter (33), the Trp, Glu, or His mutant versions (all FLAG-tagged for immunoblot detection) in the context of a chimeric protein, CBm, which consists of the CarH$_{Bm}$ C-terminal domain fused through its linker to the DBD of CarH$_{Mx}$. This was prompted by EMSA analysis showing that CarH$_{Bm}$ binds less efficiently to the CarH$_{Mx}$ operator than CBm (Fig. S5E). WT CBm, like CarH$_{Mx}$ used as positive control, restored repression of carotenogenesis in the dark (on plates containing AdoCbl and the vanillate inducer) and thereby the yellow colony color of normal WT cells (Fig. 3D), which is due to a noncarotenoid pigment DKxanthene (34). By contrast, none of the four mutants was functional *in vivo* (Fig. 3D) despite being stably expressed, as confirmed in immunoblots with anti-FLAG antibodies (Fig. 3E). Altogether, these data demonstrate that the Trp, Glu, and His of the W-X_9-EH motif in CarH$_{Bm}$ are important for AdoCbl-dependent operator binding *in vitro* and repressor activity *in vivo*.

CarH$_{Bm}$ lacks the ability of CarH$_{Tt}$ to trap bound photolyzed AdoCbl via bis-His ligation

A notable feature in light-exposed CarH$_{Tt}$ is that His-132, which flanks Trp-131 of the W-X_9-EH motif, ends up as the upper cobalt axial ligand, and the resulting bis-His-ligated photolyzed Cbl cannot escape even under harsh experimental conditions (9, 10) (Fig. 3A). Bis-His formation may have roles in possible mechanisms to trap, recover, and reuse Cbl, and in CarH$_{Tt}$ photochemistry (9, 10, 12, 24). However, His-132 is not conserved in all CarH homologs (12), including CarH$_{Bm}$, in which a Glu (Glu-144) replaces the His (Fig. S1D). Mass spectrometry of dark- and light-exposed CarH$_{Bm}$ yielded the same molecular mass, in contrast to light-exposed CarH$_{Tt}$, whose mass exceeded that of the dark form by 1329 Da due to the tightly bis-His-ligated photolyzed Cbl (Fig. 3F) (9, 10). Also, fresh AdoCbl could replace the bound Cbl in light-exposed CarH$_{Bm}$ and restore its DNA-binding (Fig. 3G), contrary to that observed for light-exposed CarH$_{Tt}$ (9, 10). Thus, unlike CarH$_{Tt}$, CarH$_{Bm}$ does not tightly retain the bound photolyzed AdoCbl.

CarH$_{Bm}$ operators are larger but conserve the CarH$_{Tt}$ operator design and binding mode

Structural and mutational analyses established that the CarH$_{Tt}$ operator comprises three ~11-bp tandem DRs, each with the sequence 5'-nnnnTnnACAn-3' (*n* is any base) in the sense strand (9, 12) (Fig. S6A). In the central DR, the conserved TnnACA forms part of the −35 promoter element (TTGACA), which is occupied by one DBD of CarH$_{Tt}$ to sterically block access to RNAP-σ^A and thereby prevent transcription initiation (9). The structure of the CarH$_{Tt}$-DNA complex revealed that the DNA recognition helix contacts the T of the TnnACA motif and the TGT complementary to ACA in the major groove, and mutating the T or AC in two DRs abolished DNA binding (9). In a previous report, a 28-bp imperfect palindrome with two 6-bp half-sites, separated by 16 bp, was proposed for both CarH$_{Bm}$ operators (25). However, we could discern 11-bp tandem DRs with the characteristic TnnACA of the CarH$_{Tt}$ operator at both CarH$_{Bm}$ target promoters (12): four at P$_{carH}$ (DR1-DR4, in the sense strand, with DR4 overlapping the −35 promoter region) and three at P$_{crtI}$ (DR1−DR3, in the antisense strand, with DR3 overlapping the −10 promoter region) (Figs. S2C and S6A).

To test experimentally if the above DRs constitute the CarH$_{Bm}$ operator, we performed DNase I, hydroxyl radical, and Exo III footprint analyses. At P$_{carH}$, CarH$_{Bm}$ yielded a DNase I footprint of ~50 bp precisely matching the span of DR1−DR4 (Fig. 4, A and B). Interestingly, the footprint at P$_{crtI}$ was also ~50 bp, spanning the region from DR1 to DR3 plus an additional ~10 bp segment downstream of DR3 that was footprinted more tenuously. This additional segment has TnnTTA instead of TnnACA, and hence can be considered a pseudorepeat that we denote dr4 (Fig. 4, A and B). The presence of four DNase I-hypersensitive sites (typically indicative of local bends toward the major groove (35)) on each probe suggests that CarH$_{Bm}$ induces DNA bending upon binding (Fig. 4, A and B). Because the hypersensitive sites occur on different strands, antisense at P$_{carH}$ but sense at P$_{crtI}$, CarH$_{Bm}$ likely binds to

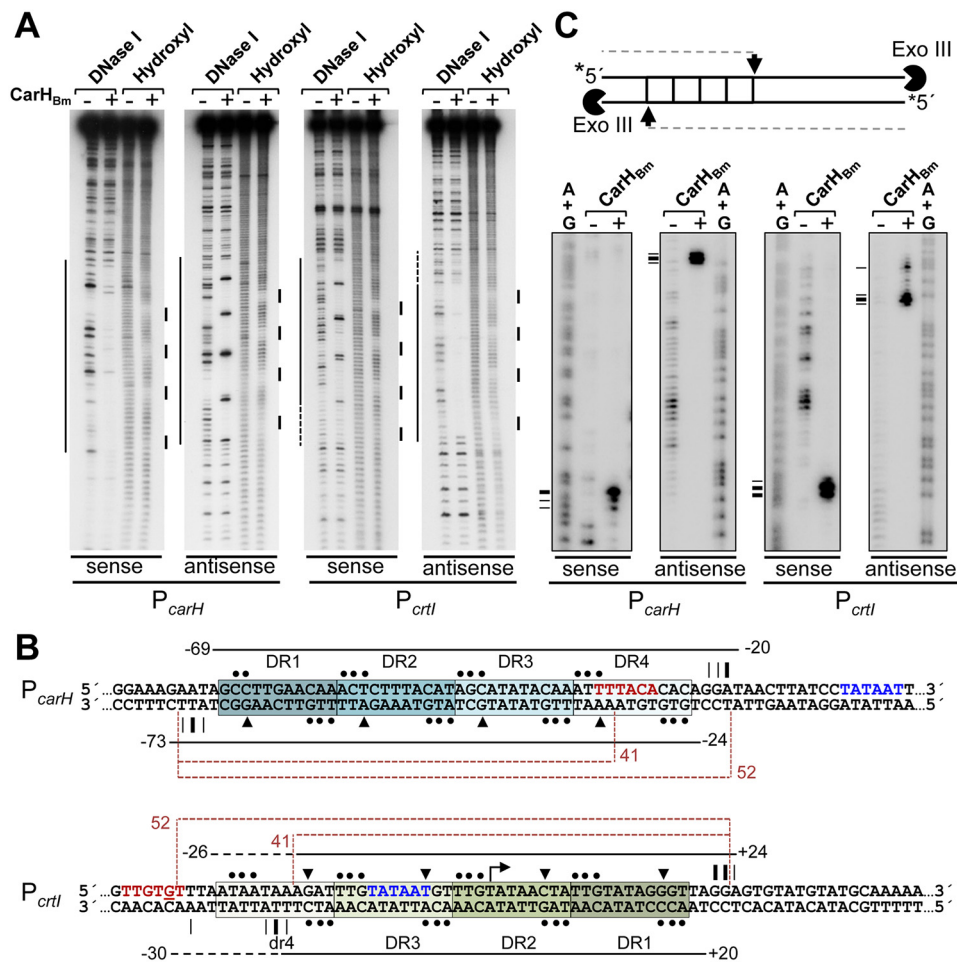![ASBMB]

J. Biol. Chem. (2018) 293(46) 17888–17905 **17893**

Figure 4. CarH_Bm footprints at the PcarH and PcrtI promoter regions. *A*, representative DNase I and hydroxyl radical footprinting in the dark on the sense and antisense strands of a 170-bp P*carH* or P*crtI* probe without or with CarH_Bm (400 nM with 5-fold molar excess of AdoCbl) present. Footprinted regions, mapped using (A+G) chemical sequencing run in parallel, are indicated by *lines* on the *left* (DNase I) and *right* (hydroxyl radical). *B*, DNA sequence of the segment containing the CarH_Bm-binding site at P*carH* and P*crtI*, with footprint data depicted for each strand (sense, above; antisense, below). *Horizontal lines* extend over regions protected against DNase I (*dashes* indicate weak protection), with limits numbered relative to the TSS. *Triangles* point to DNase I-hypersensitive sites, and *dots* to the sites protected from hydroxyl radical attack. Positions at which Exo III advance is arrested, from *C*, are indicated by *vertical lines* (thicker for stronger arrest). Each DR is *boxed* and *shaded*; repeats at P*crtI* are oriented opposite to transcription (dr4 in lowercase indicates a pseudorepeat described in the text). The −35 (in *red*) and −10 (in *blue*) promoter elements are indicated. *Dashed brown lines* indicate the span of the 52- and 41-bp probes used in Fig. 5. *C*, Exo III footprint data for CarH_Bm binding to P*carH* or P*crtI*. Scheme on *top* shows the position of Exo III arrest (*arrow*) and product size from a given strand (³²P-labeled at the 5′-end) that would be expected if the protein binds to four DRs (*squares*). Radiolabeled probe, free or preincubated in the dark with CarH_Bm (400 nM plus 5-fold molar excess of AdoCbl), was treated with Exo III and analyzed as described under supporting data. *Horizontal dashes* on the *left* point to positions of Exo III arrest (summarized in *B*) mapped using the corresponding A+G sequence ladder.

opposite sides of the DNA at the two operators, consistent with the DRs being oriented oppositely at the two sites (Fig. 4*B*). In the crystal structure, CarH_Tt binds to one face of the DNA using only three of its four DBDs; accordingly, hydroxyl radical footprinting revealed on each strand three evenly spaced protected tracts (~4-bp each), which correlated with where the "wings" of the DBDs contact the minor groove (9). CarH_Bm binding to P*carH* or P*crtI* produced on both strands four hydroxyl radical footprints (~3-bp each; Fig. 4, *A* and *B*) evenly distributed at intervals similar to those observed for CarH_Tt at its operator (9). This suggests that CarH_Bm conserves the CarH_Tt operator design and DNA-binding mode but binds to larger, four-repeat operators presumably using all four of its DBDs. This inference was further supported by Exo III footprinting (Fig. 4*C*). CarH_Bm binding to P*carH* blocked Exo III progress at about positions −19 and −71 on the sense and antisense strands, respectively (Fig. 4, *B* and *C*; numbers relative to the transcription start site,

TSS), which coincide with the limits of the DNase I footprint (Fig. 4*B*). At P*crtI*, CarH_Bm arrested Exo III at about position +24 in the sense strand, and at about positions −28 (weakly) and −19 (strongly) in the antisense strand (Fig. 4, *B* and *C*), again consistent with the ends of the DNase I footprint. That Exo III can nibble into the segment from position −28 to −19 at P*crtI*, corresponding to dr4, suggests that CarH_Bm binds weakly to this pseudorepeat.

EMSA using 52-bp P*carH* and P*crtI* DNA probes corresponding to the DNase I/Exo III footprints (the four repeats plus the 4 bp flanking each end; Fig. 4*B*) confirmed that this segment is both necessary and sufficient for CarH_Bm binding (Fig. 5*A*, Fig. S2*D*). However, DNA binding was abolished on truncating DR4 at P*carH* and diminished when dr4 at P*crtI* was truncated, consistent with dr4 being a weaker affinity site for CarH_Bm (Figs. 4*B* and 5*A*). Binding to both 52-bp probes was cooperative (Hill coefficients *n* >1) with dissociation constants K_D of (96 ± 3) nM
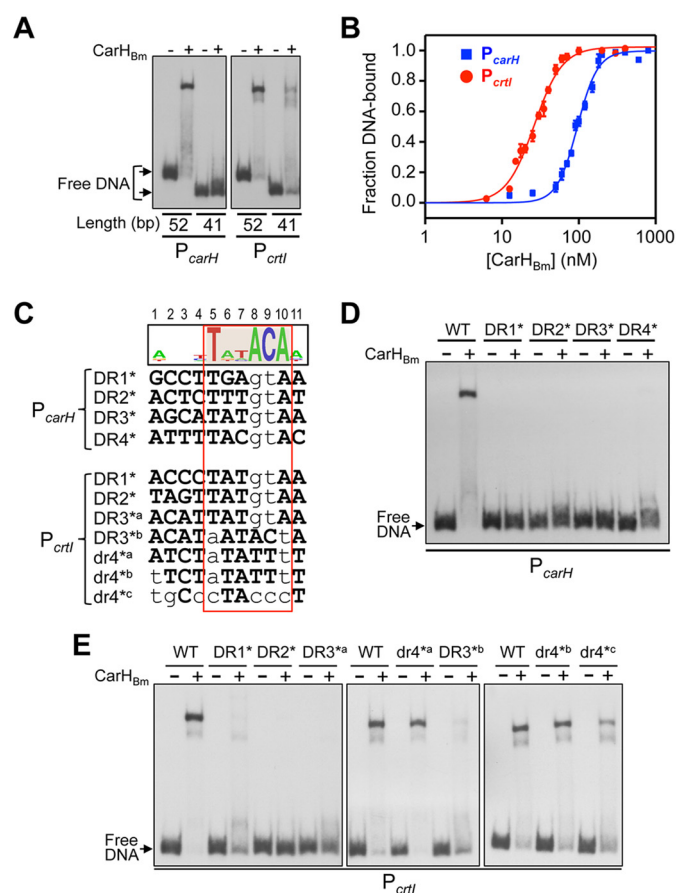
Figure 5. Analysis of CarH$_{Bm}$ binding to its operators at PcarH and PcrtI.
A, EMSA of CarH$_{Bm}$ binding to 52- and 41-bp P$_{carH}$ and P$_{crtI}$ probes correspond-ing, respectively, to all four repeats or only the first three (DR1 to DR3; Fig. 4B). CarH$_{Bm}$ was at 400 nM with P$_{carH}$ and at 50 nM with P$_{crtI}$, and AdoCbl was at a 5-fold molar excess. *B*, CarH$_{Bm}$ binding affinities to the 52-bp P$_{carH}$ (*blue*) and P$_{crtI}$ (*red*) probes from EMSA titrations (representative EMSA in Fig. S6B). Lines are fits of the data to the Hill equation with K_D, the dissociation constant, and Hill coefficient being, respectively, (96 ± 3) and (3.3 ± 0.3) nM for P$_{carH}$, and (26 ± 1) and (2.39 ± 0.2) nM for P$_{crtI}$. Mean values and standard errors from three EMSA are shown. *C*, CarH$_{Bm}$ operator repeats at P$_{carH}$ and P$_{crtI}$ aligned with mutations (*lowercase*) tested in *D* and *E*. Sequence logo on the *top* (with positions numbered) is based on the four DRs of P$_{carH}$ and DR1 to DR3 of P$_{crtI}$. The TnnACA motif is *shaded orange* in the logo and outlined by the *box in red*. *D*, EMSA of CarH$_{Bm}$ binding to 52-bp P$_{carH}$ mutant DNA probes. *E*, EMSA of CarH$_{Bm}$ binding to 52-bp P$_{crtI}$ mutant DNA probes. CarH$_{Bm}$ in *D* and *E* was 400 nM and 50 mM, respectively, with a 5-fold molar excess of AdoCbl.

for P$_{carH}$ and (26 ± 1) nM for P$_{crtI}$ (Fig. 5B, Fig. S6B). Thus, CarH$_{Bm}$ binds with higher affinity to its operator at P$_{crtI}$, despite weaker binding at dr4. By comparison, CarH$_{Tt}$ can bind to a 41-bp probe corresponding to its three-repeat operator, and its K_D of (67 ± 2) nM (9) falls in the range observed for CarH$_{Bm}$ at its two operators.

To test the role of interactions with individual bases, we per-formed EMSA with probes bearing specific mutations. Mutat-ing AC in any one of the P$_{carH}$ TnnACA motifs was sufficient to abrogate CarH$_{Bm}$ binding, emphasizing the importance of this AC and of each of the four DRs at this operator for binding (Fig. 5, C and D). Likewise, mutating AC of DR1, DR2, or DR3 at P$_{crtI}$ markedly impaired CarH$_{Bm}$ binding (Fig. 5, C and E). Because AC is not conserved in dr4 at P$_{crtI}$, we mutated the first T and the last A of its TnnTTA motif (dr4*^{a}; Fig. 5C). But, surpris-ingly, this had no effect, unlike the equivalent mutation in DR3

(DR3*^{b}), which did diminish CarH$_{Bm}$ binding (Fig. 5E); nor did an additional change of the A at the first position of dr4 to T (dr4*^{b}; Fig. 5, C and E). Because dr4 is the most AT-rich of the P$_{carH}$ or P$_{crtI}$ repeats, we also tested the effect of modifying it to be more GC-rich (dr4*^{c}; note that this GC-rich segment corre-sponds to that immediately downstream of the three-repeat CarH$_{Tt}$ operator, as will be discussed below). This decreased CarH$_{Bm}$ binding somewhat (Fig. 5E), suggesting that the con-tribution of dr4 may rest on its AT-rich nature.

In sum, the above data indicate that CarH$_{Bm}$ and CarH$_{Tt}$ share the same basic operator design, comprising tandem 11-bp DRs with a TnnACA motif, and DNA-binding mode. However, both CarH$_{Bm}$ operators are larger than that of CarH$_{Tt}$ by one repeat or pseudorepeat.

CarH$_{Bm}$ recognition of the smaller CarH$_{Tt}$ operator suggests flexible DNA binding

CarH$_{Bm}$ operators have four DRs, compared with three DRs for CarH$_{Tt}$ (9). Yet, EMSA revealed that CarH$_{Bm}$ binds to P$_{carH}$(Tt), and CarH$_{Tt}$ to both P$_{carH}$ and P$_{crtI}$ (Fig. 6A). We ana-lyzed this further by DNase I and Exo III footprinting, using P$_{carH}$(Tt) and P$_{carH}$. In contrast to its ~50-bp DNase I footprint at P$_{carH}$, CarH$_{Bm}$ yielded an ~41-bp footprint at P$_{carH}$(Tt), sim-ilar to that produced by CarH$_{Tt}$ (9) (Fig. 6, B and C); Exo III footprints were also very similar at P$_{carH}$(Tt) and matched the limits of the DNase I footprints (Fig. 6, C and D). Thus, CarH$_{Bm}$ can recognize the CarH$_{Tt}$ operator even though its natural operators are larger by one DR or pseudorepeat. Either CarH$_{Bm}$, like CarH$_{Tt}$, uses only three of its four DBDs to bind to the CarH$_{Tt}$ operator or, alternatively, the fourth DBD interacts with an adjacent segment nonspecifically, eluding detection by footprinting. In favor of the first possibility is that the GC-rich segment immediately downstream of DR3 at the CarH$_{Tt}$ oper-ator does not appear to contribute to CarH$_{Bm}$ binding, because using it to replace dr4 at P$_{crtI}$ (mutant dr4*^{c}; Fig. 5E) had the same effect as deleting dr4 (Fig. 5A).

CarH$_{Tt}$ binding at P$_{carH}$ yielded a clear DNase I footprint covering the ~41-bp segment from DR1 to DR3, and a faintly protected region extending over DR4 (Fig. 6, B and C). Accord-ingly, CarH$_{Tt}$ produced strong Exo III arrests at the limits of the ~41-bp DNase I footprint, and weak ones delimiting the stretch from DR2 to DR4 (Fig. 6, C and D). This suggests that CarH$_{Tt}$ continues to bind to three DRs even when a fourth is available and, interestingly, with a marked preference for the three upstream DRs, DR1 to DR3. To further reinforce these conclusions, we designed an artificial operator with four DRs derived from P$_{carH}$(Tt), P$_{carH}$(Tt)4r (Fig. S7A). EMSA showed that both CarH$_{Bm}$ and CarH$_{Tt}$ bind to P$_{carH}$(Tt)4r, whereas DNase I and Exo III footprinting results closely mirrored those obtained with P$_{carH}$ (Fig. S7, B–D).

Taken together, the data suggest that CarH$_{Bm}$ binds to four DRs when available but can also recognize just three, whereas CarH$_{Tt}$ binds primarily to three DRs even when a fourth is present, with a preference for the three upstream. The latter suggests positioning determinants for binding, whose nature remains to be established.
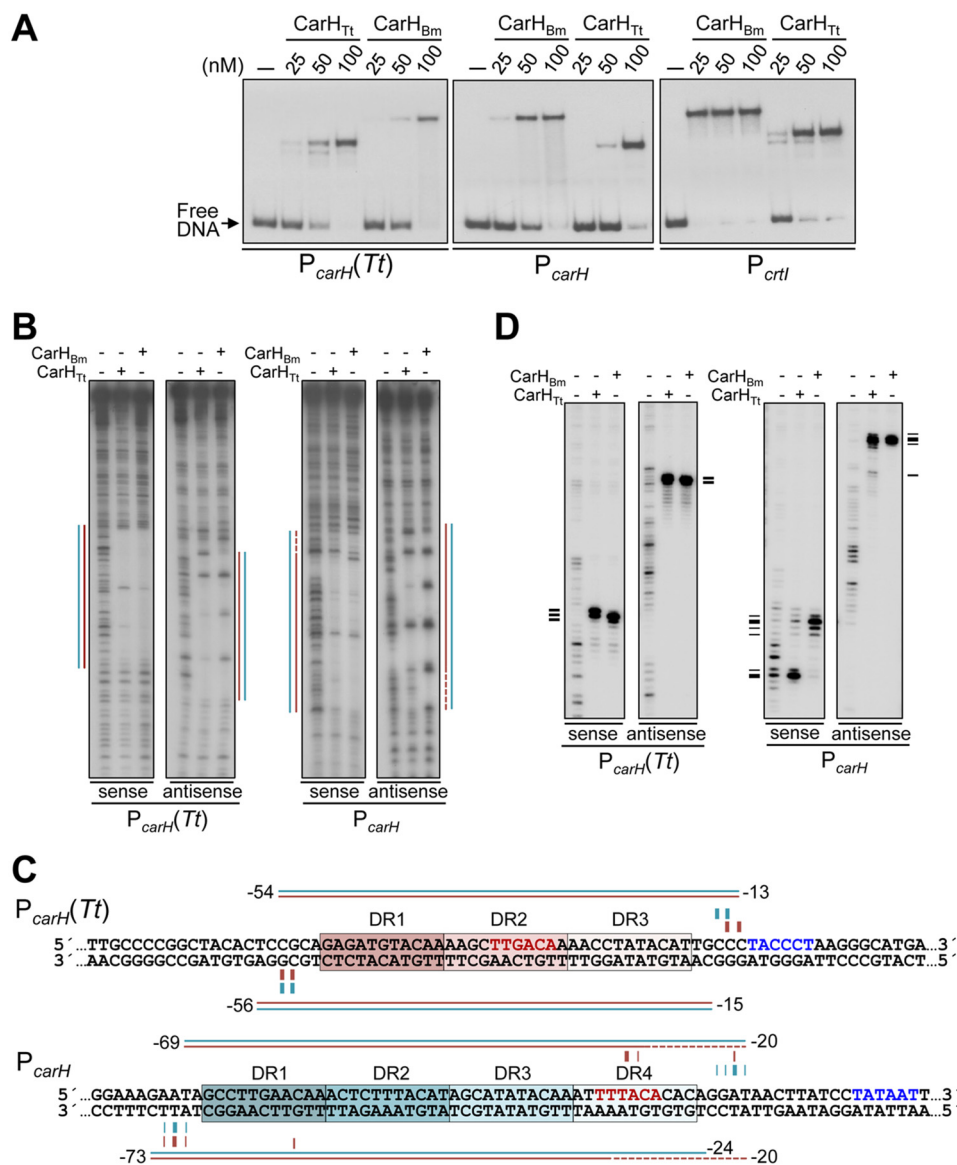
Figure 6. Binding of CarH$_{Bm}$ to the CarH$_{Tt}$ operator and CarH$_{Tt}$ to the CarH$_{Bm}$ operators. *A*, EMSA for CarH$_{Bm}$ and CarH$_{Tt}$ binding in the dark to the 170-bp operator probes P$_{carH}$(*Tt*), P$_{carH}$, and P$_{crtI}$ at the indicated protein concentrations and with AdoCbl at a 5-fold molar excess. Slower mobility of the DNA complex for CarH$_{Bm}$ may be due to size, charge, and shape differences from CarH$_{Tt}$. *B*, DNase I footprints at P$_{carH}$ (*Tt*) and P$_{carH}$ generated by the binding of CarH$_{Bm}$ or CarH$_{Tt}$ (400 nM protein with 5-fold molar excess of AdoCbl present in the dark). Lines indicating the footprint for CarH$_{Bm}$ (*cyan*) and CarH$_{Tt}$ (*pink*) were mapped using (A+G) chemical sequence ladder of the corresponding strand. *C*, sequences with footprint data summarized (*cyan* for CarH$_{Bm}$, *pink* for CarH$_{Tt}$) above and below the corresponding strands, with *horizontal lines* spanning the DNase I footprint (dashes indicating weak protection) and *vertical lines* at positions with Exo III blocked (thicker for stronger arrest). The −35 and −10 promoter elements are in *red* and *blue*, respectively, and each DR is *boxed* and *shaded*. *D*, Exo III footprint data for the binding of CarH$_{Bm}$ or CarH$_{Tt}$ (400 nM, 5-fold molar excess of AdoCbl) to P$_{carH}$(*Tt*) and P$_{carH}$. *Horizontal dashes* on the *left* align with the positions of Exo III arrest mapped using the corresponding A+G sequence ladder and summarized in *C*.

Interdomain linker effects on operator DNA binding

Why CarH$_{Tt}$ binds only to three repeats at a time, whereas CarH$_{Bm}$ can bind more flexibly to three or four repeats may be related to its longer linker between the DNA- and the AdoCbl-binding domains. Compared with the 4-residue CarH$_{Tt}$ linker (QEVR, residues 76–79), sequence alignment and the available CarH$_{Tt}$ structures (Fig. S1*D*) indicate a 16-residue linker segment (ESSTVGTFEEEGEVDS, residues 76–91) in CarH$_{Bm}$. Both linkers are predicted as unstructured (Fig. S2*B*), as was observed in the CarH$_{Tt}$ structures (9). To check for linker effects we performed steered MD simulations (36) of the CarH$_{Tt}$- and CarH$_{Bm}$-DNA complexes (supporting data). For this, CarH$_{Bm}$ and its P$_{carH}$ operator DNA were modeled to pre-

serve the mode of interaction between the DBDs and DNA, as well as the DNA curvature observed in the CarH$_{Tt}$-DNA structure (PDB code 5C8E). In the steered MD simulations, exploration of the configurational space for the DNA-bound and unbound states of the fourth DBD binding to DR4 indicated that CarH$_{Bm}$ can bind DR4 through its fourth DBD as a consequence of its longer linker, as manifested by the peak in density close to the reference bound state (~1 Å; Fig. 7*A*). By contrast, CarH$_{Tt}$ was unable to bind DR4 due to its shorter linker, with configurations displaying maximum density far from the reference bound state (~8 Å; Fig. 7*A*).

To experimentally test linker effects on DNA binding, we generated CarH$_{Bm}$ with 12 C-terminal residues of its linker
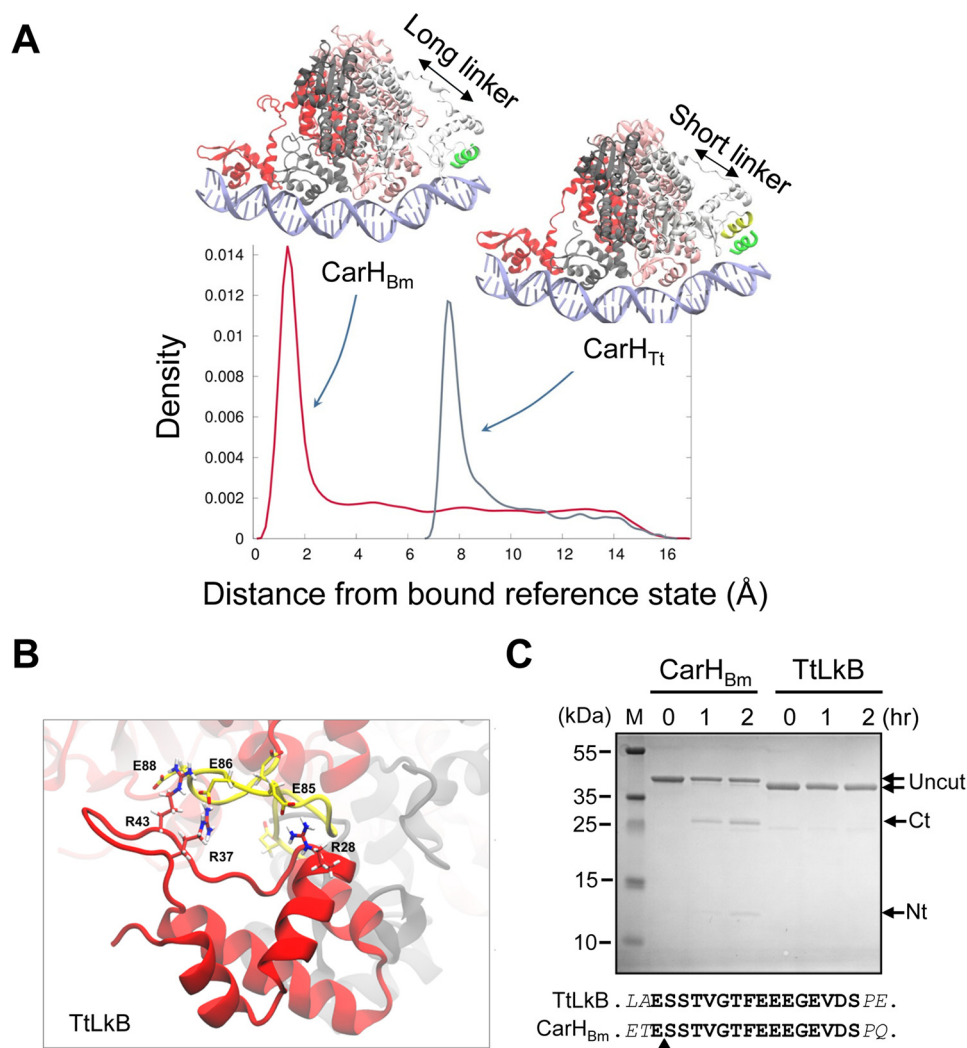
Figure 7. Linker effects on CarH$_{Bm}$, CarH$_{Tt}$, and TtLkB. *A*, density plots showing the probability to find the fourth DBD in the configurational space between 0 and 15 Å of root mean square deviation relative to the reference bound state defined by the DNA recognition helix (*green*) for CarH$_{Tt}$ and CarH$_{Bm}$, as indicated. *B*, snapshot of the last 50 ns of the 500-ns MD simulation of TtLkB showing H-bond interactions formed between the DBD Arg residues (*red*) and the Glu residues in the interdomain linker (*yellow*), as indicated. *C*, CarH$_{Bm}$ and TtLkB digested with Glu-C at the times (in hours) indicated. The uncut protein (TtLkB, 34.3 kDa; CarH$_{Bm}$, 36.3 kDa) and the GluC cleavage products (*Ct* corresponds to the C-terminal domain of CarH$_{Bm}$ (∼25 kDa) and *Nt* to the His-tagged N-terminal domain (∼12 kDa)); *M*, size markers. The sequence of the CarH$_{Bm}$ linker (*boldface*) with the two flanking residues (*italics*) in CarH$_{Bm}$ and TtLkB is shown *below*; the *arrowhead* points to the GluC-cleavage site in the linker in CarH$_{Bm}$ identified by N-terminal sequencing.

truncated so as to be of the same length as in CarH$_{Tt}$, or with its linker swapped for that of CarH$_{Tt}$, and CarH$_{Tt}$ with its linker swapped for that of CarH$_{Bm}$. Both CarH$_{Bm}$ variants with four-residue linkers tended to precipitate. This precluded their further analysis but nonetheless indicated that the linker is not a passive tether but can affect CarH$_{Bm}$ behavior in solution. On the other hand, CarH$_{Tt}$ with its linker swapped for that of CarH$_{Bm}$ (hereafter denoted TtLkB) was well behaved in solution and, like native CarH$_{Tt}$, formed AdoCbl-bound tetramers in the dark and monomers in the light or in the apo form (Fig. S8, *A–D*). We therefore tested its DNA binding to P$_{carH}$(*Tt*) and P$_{carH}$. Strikingly, no retarded band was detected in the EMSA for TtLkB binding to either probe, in contrast to CarH$_{Tt}$ (Fig. S8*E*) or CarH$_{Bm}$ (Fig. 6*A*).

On probing linker effects by unrestrained MD simulations of the AdoCbl-bound TtLkB and CarH$_{Bm}$ systems, we observed that the DBD residues Arg-28, Arg-37, and Arg-43, which are known to interact with DNA (9), were sequestered by the highly

acidic linker (calculated pI = 3.4) in the TtLkB system (Fig. 7*B*, Fig. S9), and could thereby prevent binding to DNA. By contrast, these sequestering interactions were not observed with the CarH$_{Bm}$ system (Fig. S9). Moreover, comparison of the H-bonds formed between the interdomain linker and the rest of the protein during the simulation indicated, on average, 57 ± 5 H-bonds (of which 8 ± 1 were salt bridges) for CarH$_{Bm}$, but a much higher 75 ± 6 H-bond interactions (17 ± 2 salt bridges) for TtLkB. This may rationalize, at least in part, why the linker in CarH$_{Bm}$ does not interfere with DNA binding, whereas the same linker in TtLkB prevents DNA binding possibly by interacting strongly with the DBD. Such charge interactions would be expected to shield the linker in TtLkB, more than in CarH$_{Bm}$, from proteolysis. We tested this by treating AdoCbl-bound TtLkB and CarH$_{Bm}$ with *Staphylococcus aureus* endoproteinase GluC, which preferentially cleaves accessible peptide bonds C-terminal to Glu residues. CarH$_{Bm}$ and TtLkB have many Glu residues (29 and 34, respectively) distributed along

the sequence (including those in the linker), but structural constraints may protect most of them from GluC cleavage. Consistent with interactions protecting the linker in TtLkB, no cleavage was apparent on GluC treatment of TtLkB; in contrast, GluC cleaved at the linker in $CarH_{Bm}$ to yield detectable levels of the C-terminal AdoCbl-binding and N-terminal DNA-binding domains, as confirmed by N-terminal sequencing (Fig. 7*C*). Altogether, these data indicate that linker length, composition and the context in which it occurs are important determinants of the properties of CarH photoreceptors and, importantly, of their binding to DNA.

A multipartite $CarH_{Bm}$ operator for photoregulated expression of an Spx global redox-response transcription factor

The data above showed that $CarH_{Bm}$ can recognize three or four 11-bp tandem DRs, each with a conserved T*nn*ACA motif. We therefore scanned the *B. megaterium* genome *in silico* for sites corresponding to three tandem repeats of the sequence 5′-*nnnn*T*nn*ACA*n*-3′. This yielded, besides the two known sites at P*carH* and P*crtI*, three new hits (Fig. S10*A*). One of these hits was 43 bp upstream of an isolated gene encoding an Spx family global RNAP-binding transcription regulator homolog, which is highly conserved in the phylum Firmicutes and is implicated in oxidative and other stress responses (26, 27). We refer to this gene as *spxA2* to distinguish it from the paralog, also annotated *spxA*, that we denote as *spxA1* and whose product is 86% identical in sequence to *Bacillus subtilis* Spx (Fig. S10*B*). The second new hit was 193 bp upstream of the gene for replication initiator protein DnaA, and the third was 208 bp upstream of a gene for a putative hemolysin III family protein and 161 bp upstream of a gene for a putative helix-turn-helix protein transcribed in the opposite direction. We first tested if the new hits were genuine $CarH_{Bm}$-binding sites by EMSA using 170-bp DNA probes (P*spxA2*, P*dnaA*, and P*hlyIII*). Whereas P*spxA2* was completely retarded by 50 nM $CarH_{Bm}$ and light disrupted the binding, no binding was detected to the other two probes even at $CarH_{Bm}$ concentrations as high as 1.6 μM (Fig. 8*A*). These results suggested that, of the three new hits, only P*spxA2* may be subject to light-dependent regulation by $CarH_{Bm}$. Consistent with this, quantitative RT-PCR (qRT-PCR) analysis revealed that expression of *spxA2*, but not of *dnaA* or *hlyIII*, was induced by light to levels comparable with the positive control *crtI* (Fig. 8*B*). Moreover, in a *carH_{Bm}*-deleted mutant, *spxA2* exhibited high-level expression in the dark or light, like *crtI* and unlike *dnaA* (Fig. 8*B*). This further supports that $CarH_{Bm}$ mediates the photoregulated expression of *spxA2.* These results thus validated the hit at P*spxA2*. On the other hand, they also indicated that three tandem 5′-*nnnn*T-*nn*ACA*n*-3′ repeats as query is not sufficiently stringent to identify $CarH_{Bm}$ binding sites.

DNase I footprinting analysis of $CarH_{Bm}$ binding to P*spxA2* yielded, surprisingly, an ~70 bp footprint (with six hypersensitive sites in the antisense strand), about twice the expected size for a three-repeat site, and also larger than the footprints observed at P*carH* and P*crtI* (Fig. 8, *C* and *D*). Besides the three tandem DRs identified in the genome-wide search (DR3, DR4, DR5; Fig. 8*C*, Fig. S10*A*), we discerned in the footprint an additional DR (DR1) and a pseudorepeat (dr2) upstream of DR3,

and another pseudorepeat (dr6) downstream of DR5. DR1 is identical to DR4; dr2, spaced 1-bp away from DR3, resembles DR5 except at positions 4 and, importantly, 8, where G replaces the first A of the T*nn*ACA motif; and dr6, footprinted more weakly, has A instead of C of the motif (Fig. 8, *C* and *H*). Because the four DBDs of a $CarH_{Bm}$ tetramer can bind at most four DRs at a time, we investigated further how $CarH_{Bm}$ recognizes the composite site at P*spxA2*. First, $CarH_{Bm}$ blocked Exo III (Fig. 8, *C* and *E*) in the sense strand within DR5 (strongly) and dr6 (strongly), and downstream of dr6 (weakly); and in the antisense strand upstream of DR1 (strongly), and within DR1 (weakly) and dr2 (modestly). This suggested that $CarH_{Bm}$ can bind to three four-repeat segments at P*spxA2*, from DR1 to DR4, dr2 to DR5, and DR3 to dr6. Consistent with this, $CarH_{Bm}$ could bind well to probes corresponding to each of these four-repeat segments (Fig. 8*F*, *top gels*), and with comparable affinities (Fig. 8*G*): K_D of (17.9 ± 0.8) and (29.8 ± 1.8) nM, respectively, for DR1−4 and DR2−5, despite the 1-bp spacing between dr2 and DR3 in both 53-bp probes, and of (17.3 ± 0.7) nM for the 52-bp probe DR3−6. As expected, light disrupted this binding (Fig. S10*C*). By contrast, binding was weaker with probes having only three repeats, being most evident with the 42-bp probes DR1−3, DR2−4, and DR4−6, which have two DRs and one pseudorepeat, and less so with the 41-bp DR3−5 probe, with three DRs (Fig. 8*F*, *bottom gels*). The $CarH_{Bm}$ operator at P*spxA2* thus appears to be multipartite, with three overlapping binding sites, each one made up of three DRs and one pseudorepeat. Notably, the change in register expected from the 1-bp spacing between two contiguous repeats in two of the sites does not impair $CarH_{Bm}$ binding. Importantly, all three sites would include the putative −35 promoter element (assigned tentatively based on comparison with P*carH* and P*crtI*), with DR3-dr6 also including the putative −10 promoter element (Fig. 8*C*).

As with the three sites at P*spxA2*, we could identify a pseudorepeat in tandem downstream of DR3 at P*dnaA*, and a DR separated by 1 bp downstream of DR3 at P*hlyIII* (Fig. S10*A*). Yet, even at high $CarH_{Bm}$ concentrations no binding was detected at P*dnaA* or P*hlyIII*, as noted before (Fig. 8*A*), suggesting that this cannot be attributed to lack of a fourth DR or pseudorepeat. Hence, we reasoned that binding or otherwise to $CarH_{Bm}$ depends on additional sequence information within the DRs, besides the conserved T*nn*ACA motif. In other words, the less conserved bases also contribute, as was observed with $CarH_{Tt}$ in the structure of its complex with DNA (9). Aligning the DRs at P*spxA2* with those at P*carH* and P*crtI* yielded A*nn***TATACA**A (less conserved bases not in bold), as a more refined consensus repeat sequence for $CarH_{Bm}$ recognition (Fig. 8*H*). The deviations observed at these less conserved positions from the above consensus in one or more DRs at P*dnaA* and P*hlyIII* (for example, positions 6 and 7 in all three DRs at P*dnaA*, or position 1 in all four DRs at P*hlyIII*, among others; Fig. 8*H*) could explain why these, despite having the T*nn*ACA motif, do not bind $CarH_{Bm}$.

Discussion

Photoregulation of transcription by CarH is determined by the interplay between AdoCbl and light to modulate the oligomeric state, cooperative operator DNA binding, and repressor activity of CarH. High-resolution structural-mutational studies
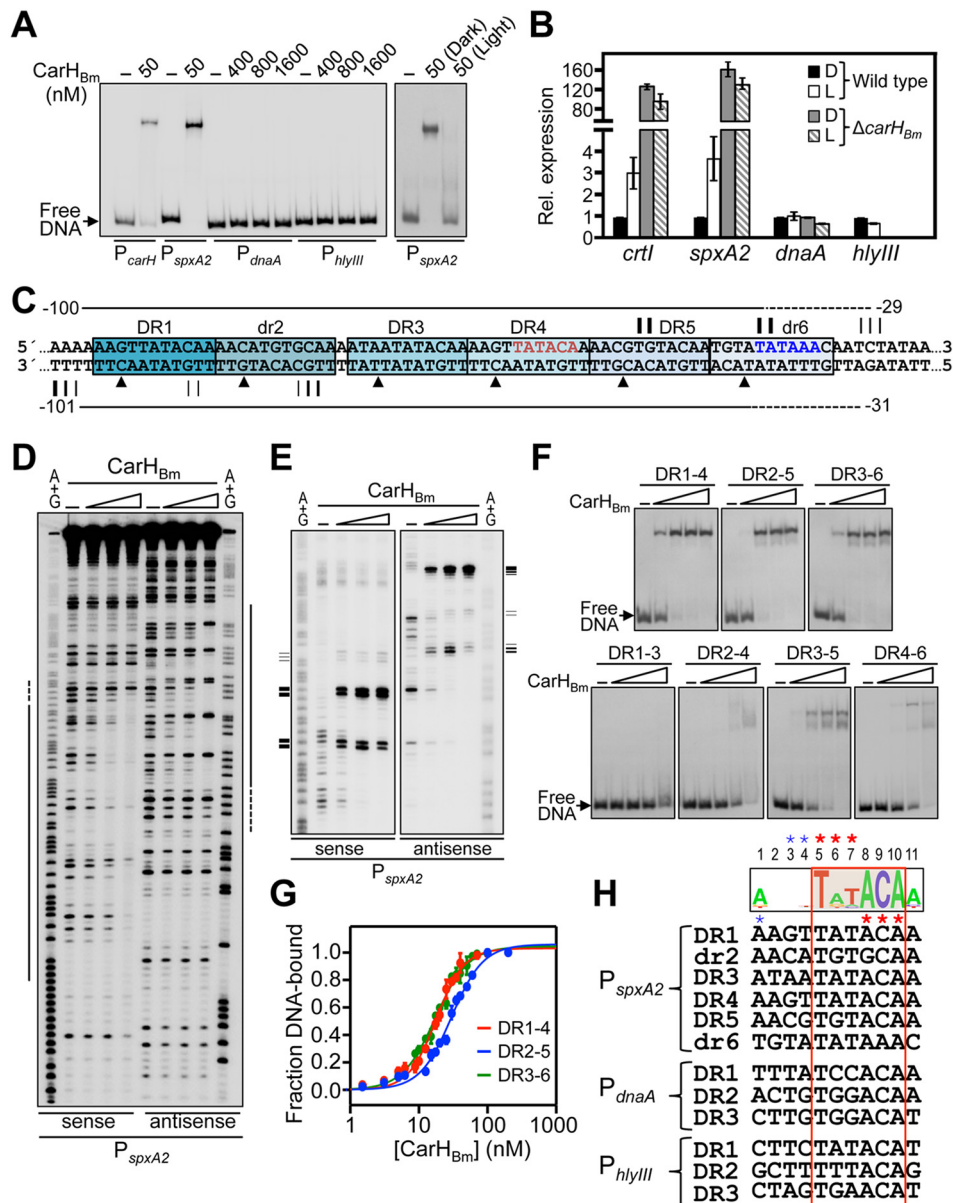
Figure 8. CarH$_{Bm}$ binding to a multipartite operator upstream of photoregulated *spxA2*. *A*, representative EMSA for CarH$_{Bm}$ binding to 170-bp probes P$_{spxA2}$, P$_{dnaA}$, and P$_{hlyIII}$. Binding to P$_{carH}$ is shown for comparison. The effect of green light on binding at P$_{spxA2}$ is shown in the *right panel*. Protein concentrations indicated on *top* have AdoCbl at a 5-fold molar excess. *B*, qRT-PCR analysis of *crtI* (positive control), *spxA2*, *dnaA*, and *hlyIII* expression in WT and *carH*$_{Bm}$-deleted *B. megaterium* strains grown in the dark (*D*) and light (*L*), as indicated. Mean ± S.E. of three independent measurements are shown. *C*, sequence of the CarH$_{Bm}$-binding site at P$_{spxA2}$ summarizing footprint data on each strand from *D* and *E*. *Horizontal lines* span the DNase I footprint (*dashes* for weak footprint) and *triangles* point to hypersensitive sites (from *D*). *Vertical lines* align with positions at which CarH$_{Bm}$ blocks Exo III progress, with *thicker lines* for stronger arrest (from *E*). Tentative −35 (*red*) and −10 (*blue*) promoter elements are indicated. Each DR is *boxed and shaded*. *D*, DNase I footprints in the dark on the sense and antisense strands of P$_{spxA2}$ without and with CarH$_{Bm}$ (50, 100, and 400 nM) and with a 5-fold molar excess of AdoCbl). *Lines on the side* correspond to the footprint mapped using the respective (A+G) chemical sequencing ladder. *E*, Exo III footprint data for the binding of CarH$_{Bm}$ (concentrations as in *D*) to P$_{spxA2}$. *Horizontal lines* on the *side* mark the positions of Exo III arrest (*thicker lines* for stronger arrest) mapped using the corresponding A+G sequence ladder, as summarized in *C*. *F*, EMSA for CarH$_{Bm}$ binding to P$_{spxA2}$ probes with four (top gels) or three (bottom gels) repeats. Each probe corresponds to the segment extending over the repeats indicated, as numbered, plus the 4-bp flanking each end. Increasing CarH$_{Bm}$ concentrations (25, 50, 100, and 400 nM) and a 5-fold molar excess of AdoCbl were used. *G*, EMSA titration data for CarH$_{Bm}$-binding to the four-repeat probes in *F*. *Lines* are fits of the data to the Hill equation. K_D and Hill coefficients are, respectively (17.7 ± 0.8) and (2.14 ± 0.15) nM for DR1–4; (29.8 ± 1.8) and (1.9 ± 0.2) nM for DR2–5; and (17.3 ± 0.7) and (1.8 ± 0.1) nM for DR3–6. Mean ± S.E. of three experiments are shown. *H*, alignment of repeat hits at P$_{spxA2}$, P$_{dnaA}$, and P$_{hlyIII}$, with the sequence logo based on the P$_{carH}$, P$_{crtI}$, and P$_{spxA2}$ repeats indicated on top; the TnnACA motif is *boxed in red*, with positions numbered on top. *Asterisks* indicate major groove (*red*) and minor groove (*blue*) contacts, in the sense and antisense strands, in the CarH$_{Tt}$-DNA structure (9).

of *T. thermophilus* CarH$_{Tt}$ revealed many unique facets of this photoreceptor and provided fundamental insights into its AdoCbl-binding, quaternary structure, operator design, and DNA-binding mode (9, 11). Our present analysis of *B. megaterium* CarH$_{Bm}$ reveals a conserved mode of action, with an

underlying plasticity. CarH$_{Bm}$ binds to its operators only as an AdoCbl-bound tetramer, like CarH$_{Tt}$, but differs in the oligomeric states of the apo and light-exposed AdoCbl-bound forms, neither of which bind DNA. ApoCarH$_{Bm}$ is an apparent tetramer and light-exposed CarH$_{Bm}$ is a dimer (Fig. 9), whereas
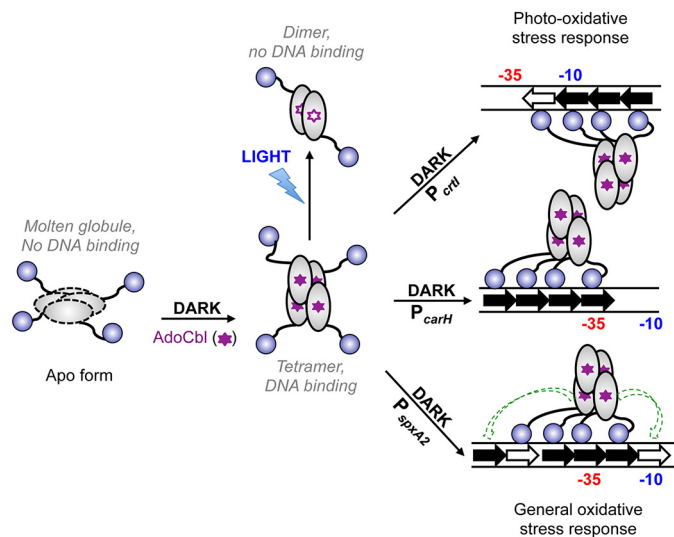
Figure 9. Model for AdoCbl- and light-dependent CarH$_{Bm}$ oligomerization, operator design, and DNA-binding mode. The oligomeric apoCarH$_{Bm}$ molten globule does not bind DNA. Its binding to AdoCbl (*filled purple stars*) in the dark produces the tetramer with the correct fold for DNA binding. Light photolyzes CarH$_{Bm}$-bound AdoCbl (*unfilled purple stars*) and induces tetramer collapse to dimers unable to bind operator DNA. *Filled arrows* indicate repeats with the TnnACA motif and *unfilled arrows* are pseudorepeats. Repeats orient in the same direction as the promoter (−35 and −10 elements indicated) at P$_{carH}$ (*middle right*) and P$_{spxA2}$ (*bottom right*), and in the opposite sense at P$_{crtI}$ (*top right*). Consequently, the CarH$_{Bm}$ tetramer binds to one DNA face at P$_{carH}$, whose operator includes the −35 promoter element, and at P$_{spxA2}$, whose multipartite operator includes both the −35 and −10 promoter elements, but to the opposite face at P$_{crtI}$, whose operator includes the −10 promoter element. The *dashed green arrows* for CarH$_{Bm}$ binding at P$_{spxA2}$ indicates two additional modes of binding to four tandem repeats on either side of that depicted at this multipartite, six-repeat operator.

the corresponding inactive forms of CarH$_{Tt}$ are monomers (11). Our data suggest that despite an oligomeric state akin to the AdoCbl-bound tetramer, apoCarH$_{Bm}$ is a molten globule with structural differences, which may explain why it cannot bind operator DNA but must associate with AdoCbl to acquire the right tetramer conformation for operator recognition.

AdoCbl binds to CarH$_{Tt}$ via crucial contacts of its 5′-dAdo upper axial moiety with a W-X_9-EH motif (9), and the ensuing allosteric changes must determine assembly of apoCarH$_{Tt}$ monomer to a tetramer. Mutating the equivalent Trp, Glu, or His in CarH$_{Bm}$ also impaired its binding to AdoCbl and function, emphasizing the critical role of this motif. It is remarkable that AdoCbl drives the transition from a monomer to the active tetramer in CarH$_{Tt}$, but from a preformed inactive tetramer to the appropriately folded tetramer in CarH$_{Bm}$. This highlights plasticity in how AdoCbl binding modulates oligomerization and activity of this family of photoreceptors, even as its requirement for the W-X_9-EH motif is conserved. As in the dark, plasticity is also observed in the transition to the light-exposed state. Light disrupts both CarH$_{Bm}$ and CarH$_{Tt}$ tetramers by photolysis of the bound AdoCbl and loss of its 5′-dAdo group, but yields CarH$_{Bm}$ dimers *versus* CarH$_{Tt}$ monomers, with both proteins retaining the photolyzed Cbl. In light-exposed CarH$_{Tt}$, the trapped Cbl resists exchange because it is held in a very tight bis-His-cobalt linkage via a nonconserved His (next to the Trp of the W-X_9-EH motif) that is not required for tetramer disassembly in the light, or assembly in the dark (9, 12). This bis-His linkage cannot form in light-exposed CarH$_{Bm}$, however,

because the equivalent residue is a Glu and, accordingly, the bound Cbl was exchangeable with intact AdoCbl *in vitro*. Although retention of photolyzed Cbl may have biological relevance in the recovery and reuse of the biologically expensive AdoCbl in some species like *T. thermophilus* (9, 12), lack of the bis-His linkage in *B. megaterium* CarH$_{Bm}$ (and in the homologs of some other species that also lack the His) can facilitate photoreceptor regeneration simply through exchange with fresh AdoCbl, allowing for more rapid cycling between dark-light states.

Our data establish that CarH$_{Bm}$ conserves the unique operator design and DNA-binding mode first discovered for the CarH$_{Tt}$ tetramer. However, the CarH$_{Bm}$ tetramer binds to a larger operator using all four DBDs (Fig. 9). Interestingly, CarH$_{Bm}$ affinity for its site at P$_{carH}$, with four tandem 11-bp DRs, is lower (K_D 4-fold higher) than for the site at P$_{crtI}$ or for any of those at P$_{spxA2}$, all with 3 DRs and a pseudorepeat; and no binding was detected at P$_{dnaA}$ and P$_{hlyIII}$, even though both have three DRs plus a pseudorepeat (at P$_{dnaA}$) or another DR (at P$_{hlyIII}$). This suggests that the less conserved bases of the $nnnn$TnnACAn consensus DR are also important for DNA recognition. Thus, it appears that the information content, from sequence variations around the conserved elements in the DRs, affords considerable plasticity in determining DNA-binding affinities. Such a plasticity would allow combinatorial use of differentially optimized DRs and/or pseudorepeats to fine-tune relative affinities and hence occupancies at different target operators, as a physiologically relevant strategy for regulation *in vivo*.

Like CarH$_{Tt}$, CarH$_{Bm}$ binds to one face of the DNA, determined by the orientation of the DRs, which is the same relative to the promoter at P$_{carH}$ and P$_{spxA2}$, but opposite at P$_{crtI}$ (Fig. 9). In line with a common DNA-binding mode, CarH$_{Bm}$ recognizes the three-DR CarH$_{Tt}$ operator and CarH$_{Tt}$ the larger four-DR CarH$_{Bm}$ operators. However, even when a fourth DR is available, CarH$_{Tt}$ still appears to bind to only three DRs, preferring the three upstream ones, hinting at positioning determinants whose nature remains to be established. That the CarH$_{Bm}$ operators house the −35 (P$_{carH}$), −10 (P$_{crtI}$), or both promoter elements (possibly at P$_{spxA2}$) suggests that CarH$_{Bm}$ binding to either region can block access to RNAP to repress transcription. This mirrors the behavior reported for the winged-helix multiple antibiotic resistance (MarR) transcriptional factor MepR dimer, which can also bind to opposite faces of inverted repeat operator DNA overlapping the −35 and/or the −10 (and the TSS) element (37).

Modeling and MD simulations suggested that the CarH$_{Bm}$ tetramer could use its fourth DBD to contact an additional repeat because its interdomain linker is longer than in CarH$_{Tt}$. The flexible, structurally disordered linker is free of contacts in the CarH$_{Tt}$ structures (9) and varies considerably in length and sequence among CarH homologs (12). Although this may suggest that the linker is a passive (albeit necessary) nonspecific tether to physically join the two functional domains, we observed profound effects of the length, sequence, and protein context of the linker on CarH solution properties and DNA binding. Understanding linker effects at a molecular level depends on obtaining high-resolution experimental data, a

challenging task for flexible, structurally disordered regions. Moreover, heterogeneity in linker length and sequence among CarH homologs also complicates comparative analysis. Hence, a more detailed analysis of linker effects will have to be pursued in future studies. Linkers, which necessarily relay allosteric effects between the structured functional domains they connect, can modulate DNA binding specificity and affinity, even when distant from the interacting surfaces, through transient and dynamic contacts with DNA (38–40). This can facilitate the search for specific sites and the final binding, as has been proposed for the DNA binding of bacterial nucleoid-associated protein H-NS (41) and eukaryotic transcription factors Oct1 and Pax6 (42, 43). Alternatively, linkers can diminish DNA binding via competing and unfavorable interactions through the presence of many acidic residues and/or phosphorylation that increase their negative charge, or through the entropic costs incurred on binding due to greater length and flexibility of linkers (38, 44). These factors may be in play in our observed linker effects on CarH binding to DNA, as was inferred from the MD simulations for CarH$_{Tt}$ with the highly acidic CarH$_{Bm}$ linker *versus* CarH$_{Bm}$.

In *B. megaterium*, as in *T. thermophilus* and *M. xanthus*, CarH orchestrates light-dependent regulation of carotenoid biosynthesis. Carotenoids are known to be an important line of defense against singlet oxygen, the primary source of photooxidative stress in microorganisms (2, 6). The discovery in this study of a CarH$_{Bm}$ operator upstream of *spxA2,* which encodes an Spx-type regulator whose expression is activated by light, not only revealed an intriguing multipartite operator but also a new target gene for regulation by CarH$_{Bm}$. Spx proteins are highly conserved factors in the phylum Firmicutes (multiple paralogs often exist and *B. megaterium* has at least one more) that interact with the RNAP α subunit to activate expression of genes involved in cellular defense against oxidative stresses (such as disulfide and peroxide stress) (27, 45). Complex regulatory mechanisms at the transcriptional and post-translational levels (use of multiple promoters, dependence on σ^A or alternative σ factors, transcriptional regulators, regulated proteolysis) have been shown to control expression of *spx* genes (26, 27) in *B. subtilis* and other Firmicutes lacking a CarH homolog. Our study reveals the first example known of an *spx* gene whose expression is photoregulated. Simultaneous regulation of carotenoid synthesis (to quench singlet oxygen and related reactive oxygen species) and of *spx* expression (to activate general oxidative stress response pathways) by CarH$_{Bm}$ would enable these two lines of defense to converge as a more effective strategy to combat oxidative cellular damage caused by light. CarH$_{Bm}$ has comparable affinities for each of the three sites comprising the multipartite operator at P$_{spxA2}$ and for that at P$_{crtI}$ but, interestingly, a 4–5–fold lower affinity for the site at P$_{carH}$. If these relative affinities correlate directly with *in vivo* occupancy, then CarH$_{Bm}$ would control its own expression less tightly than that of its other target genes. This may reflect an effective regulatory strategy in *B. megaterium* for CarH$_{Bm}$ to control target genes present at loci unlinked to that of its own gene, in contrast to *M. xanthus* or *T. thermophilus* where the known target genes occur at the same locus. The physiological basis for multiple recognition sites at P$_{spxA2}$ is unclear. It may be related to a possibly complex *spx* transcription, as in some other bacteria, and perhaps to achieve finer modulation of signal sensitivity and expression levels, as has been invoked for some other repressors (46). Future work can provide more details into these aspects and on how CarH-mediated photoregulation of Spx expression impinges on cellular physiology upon exposure to light.

Altogether, our study provides new insights into the specific binding to AdoCbl, its determinants, and oligomerization of CarH photoreceptors, and their mode of operator DNA binding. It has also uncovered a previously unsuspected role of the interdomain linker in modulating DNA binding. Moreover, the study has identified a multipartite light-dependent operator that controls expression of a global regulator of general oxidative stress responses, thereby linking it to the photooxidative stress response in *B. megaterium*. Plasticity in oligomerization, operator architecture, and DNA binding, within a conserved mode of action, thus appears to underpin how B$_{12}$-based CarH photoreceptors direct light-dependent gene regulation.

Experimental procedures

Strains, plasmids, growth conditions, and stock solutions

Bacterial strains and plasmids used in this study are listed in Table S1. *E. coli* strain DH5α was used for plasmid constructions and BL21 DE3 for protein overexpression. *Escherichia coli* and *B. megaterium* strain DSM 32/ATCC 14581 (DSMZ, Germany) were grown in LB (Luria-Bertani) liquid medium or LB-agar (1%) plates at 37 or 25/18 °C for inducing overexpression of His$_6$-tagged proteins in *E. coli*. *M. xanthus* was grown at 33 °C in CTT (casitone-Tris) medium (11). Growth media were supplemented as required with vitamin B$_{12}$ or AdoCbl (Sigma), antibiotics (50 μg ml^{-1} ampicillin; 40 μg ml^{-1} kanamycin), or vanillate (20 μM). Concentrations of Cbl stock solutions in aqueous buffer were estimated as described previously (11), and that of ANS (Fluka) from the absorbance at 350 nm using an extinction coefficient (ϵ) of 5000 M^{-1} cm^{-1} (47). Ultrapure guanidinium chloride was obtained from ICN Biochemicals. Plates or liquid cell cultures were illuminated as required with white light (three 18-watt fluorescent lamps, 10 W m^{-2}).

Plasmid and strain construction

Coding sequences for His$_6$-tagged CarH$_{Bm}$ or mutants for overexpression in *E. coli* were cloned into the NdeI and BamHI sites of the pET15b vector. The *carH$_{Bm}$* gene was PCR-amplified from *B. megaterium* genomic DNA. Genes encoding mutant versions of CarH$_{Bm}$ and its chimera CBm (with the N-terminal segment spanning residues 1 to 74 replaced by that of CarH$_{Mx}$) were synthesized (GenScript). For functional analysis *in vivo*, the coding sequence for CBm and its variants, and for CarH$_{Mx}$, fused to an N-terminal FLAG tag (for protein detection using immunoblot analysis), were cloned into plasmid pMR3679 (which confers kanamycin resistance, Km^R) to enable their conditional expression from a vanillate-inducible promoter (33). Each construct was electroporated into the *M. xanthus* strain MR2648, and transformants with the plasmid integrated at a heterologous site by homologous recombination were selected by their Km^R. All constructs were verified

by sequencing. Each strain was grown in the dark in liquid CTT media with vanillate, AdoCbl, and kanamycin, spotted on plates of the same medium and incubated in the dark or light, colony color being used to assess if the CarH$_{Bm}$ variant was functional.

For targeted deletion of *carH*$_{Bm}$ in *B. megaterium*, we used the *E. coli*-*Bacillus* shuttle vector pUCTV2 (48), which replicates stably in *B. megaterium* at 30 °C but not at 42 °C. Using genomic DNA as template and appropriate primers, ~1 kb segments upstream and downstream of *carH*$_{Bm}$ were PCR-amplified as BamHI-XhoI and XhoI-BamHI products, respectively, and then cloned into the BamHI site of pUCTV2. The construct was introduced into *B. megaterium* protoplasts by PEG-mediated transformation and selected on LB/tetracycline (10 μg ml^{-1}) plates at 30 °C, as described (49). Transformants were picked for growth at 42 °C in LB/tetracycline for plasmid integration into the genome by homologous recombination, and then in LB at 42 °C for allele exchange and loss of plasmid. Colonies bearing the *carH*$_{Bm}$ deletion were easily identified by their strong yellow color in the dark and verified by PCR.

Two-hybrid analysis

Bacterial two-hybrid analysis of light and B$_{12}$-dependent oligomerization was carried out as described previously (11). The PCR-amplified gene was cloned into the XbaI and BamHI sites of pKT25 or pUT18C; given pairs of constructs were introduced into *E. coli* strain BTH101 (*cya*$^-$) by electroporation. CarH$_{Mx}$, which depends on B$_{12}$ to self-interact, and CarA$_{Mx}$, which does not, served as controls (11), and pairs with only one fusion protein as negative controls. Interaction was assessed qualitatively from the blue color that developed on LB plates containing 40 μg/ml of X-Gal (5-bromo-4-chloro-3-indolyl β-D-galactoside) with or without 1 μM vitamin B$_{12}$ (cyanocobalamin), in the dark or light (11).

Western blot analysis

Immunoblot analysis of *M. xanthus* whole cell extracts expressing FLAG-tagged proteins was carried out as described elsewhere (50). Cell pellets from 1-ml samples from cultures grown in the dark to A_{550} ~0.7 in CTT, 1 μM AdoCbl, 20 μM vanillate were suspended in 300 μl of buffer containing cOmplete protease inhibitor (Roche Applied Science), 1 mM each benzamidine and phenylmethylsulfonyl fluoride (Sigma) and lysed with SDS/chloroform. After isolating the supernatant by centrifugation and estimating total protein (protein assay kit, Bio-Rad), aliquots with the same total protein were resolved in 10% SDS-PAGE gels, transferred to Hybond-ECL membranes, and probed using anti-FLAG M2 monoclonal antibodies and the ECL system (F3165, Sigma), with the RNAP β subunit probed with monoclonal anti-RNAP β antibody (8RB13; ThermoFisher) serving as the loading control.

Protein purification

His$_6$-tagged CarH$_{Bm}$, CarH$_{Tt}$, or variants were overexpressed using pET15b constructs in *E. coli* BL21 DE3 and purified as native apoproteins using protocols and buffers detailed in previous studies (9, 11), except for the presence of 2 mM β-mercaptoethanol in the buffers used for CarH$_{Bm}$ and its variants. Proteins purified in a final SEC step (in 150 mM NaCl, 50

mM phosphate buffer, pH 7.5, 2 mM β-mercaptoethanol) were concentrated and aliquots were frozen at −70 °C in buffer alone or with 50% glycerol. Purified protein identities were verified by SDS-PAGE and by electrospray ionization-TOF MS, as described in our previous study (9). AdoCbl in stocks and when protein-bound was always handled under red or dim light and periodically checked by UV-visible spectroscopy to rule out inadvertent photolysis. When required, samples in 1.5-ml tubes were irradiated for specific times (1–5 min) with white light (10–12 Wm^{-2} from 18-watt fluorescent lamps), at specific wavelengths (405/465 nm, *blue-violet*; 520 nm, *green*; 660 nm, *red*) using a computer-controlled LED (light-emitting diode) array with regulatable 0–20 Wm^{-2} intensities, or at 360 nm for UV using a Nikon Eclipse 80i epifluorescence microscope with UV-2E/C filter (8, 11). Light intensities were estimated using an 1815-C optical power meter equipped with an 818-SL detector (Newport). Protein concentrations were determined using the Bio-Rad protein assay kit and absorbance at 280 nm in a Cary 60 UV-visible spectrophotometer with molar extinction coefficients ϵ_{280} (in M^{-1} cm^{-1}, calculated from protein sequences (http://web.expasy.org/protparam) of 37,900 for CarH$_{Tt}$ and variants, 39,420 for CarH$_{Bm}$ and variants (33,920 for the Trp mutant), and with 22,500 added for AdoCbl in the holoprotein (9).

Analytical SEC

A Superdex200 HR 10/30 column (GE Life Sciences) equilibrated with 150 mM NaCl, 50 mM phosphate buffer, pH 7.5, 2 mM β-mercaptoethanol and an AKTA HPLC unit were used for analytical SEC. Calibration of the column as described previously (9, 11) yielded log M_r = 7.885−0.221 V_e, where M_r is the apparent molecular mass and V_e the elution volume. Pure protein (100 μl, 50–100 μM), alone or after 15-min incubation with a 5-fold molar excess of AdoCbl or MeCbl, was injected into the column in the dark or after 5-min exposure to light and the elution at a flow rate of 0.4 ml/min was tracked by absorbance at 280, 361, and 522 nm. Peaks were analyzed for M_r and by UV-visible spectroscopy and SDS-PAGE.

UV-visible absorption, CD, and fluorescence spectroscopy

UV-visible absorption spectra were recorded at room temperature in a Cary 60 UV-visible spectrophotometer. Far-UV and near-UV CD spectra were recorded at 25 °C in an Applied Photophysics (UK) Pistar unit with Peltier temperature control/Neslab RTE-70 unit and calibrated with (+)-10-camphorsulfonic acid. Fluorescence spectra were recorded at 25 °C in a Jobin-Yvon fluorimeter. Difference UV-visible absorbance (ΔA) was used to determine the binding affinity (K_D) for AdoCbl of CarH$_{Bm}$ or its H154A variant, as reported previously (10). Details of the spectroscopic measurements and analysis are provided under supporting data.

DNA-binding assays

All *in vitro* DNA-binding assays were performed under similar solution conditions in the dark or after irradiation with light, at least three times for each condition. DNA probes (170 bp) were PCR-amplified using primers, with one ^{32}P-labeled at the 5′-end with T4 polynucleotide kinase (Takara) prior to

PCR. For shorter DNA probes, complementary HPLC-purified synthetic oligonucleotides (Sigma) were mixed with one 5′-end ^{32}P-labeled using T4 polynucleotide kinase and the other unlabeled and present at a 2-fold excess, incubated at 100 °C for 2 min and hybridized by slow cooling. EMSAs, their analysis to estimate K_D, the apparent DNA-protein equilibrium dissociation constant, and DNase I and hydroxyl radical footprinting assays used procedures identical to those described in our previous study (9). Details for these and for Exo III footprinting are provided under the supporting data.

GluC proteolysis assay

Pure CarH$_{Bm}$ or TtLkB (0.3 μg/μl) were incubated in the dark with 5-fold molar excess AdoCbl in EMSA buffer lacking BSA for 30 min at 37 °C. Samples were then treated with GluC endopeptidase (Promega) at a 1:50 ratio (w/w) in 150 μl of total volume at 30 °C. Aliquots of 50 μl were withdrawn at 0, 1, and 2 h, and the reaction was stopped by adding phenylmethylsulfonyl fluoride to 1 mM. From each aliquot, 20 μl were mixed with 4 μl of 5× SDS-PAGE buffer, heated in a boiling water bath for 5 min, electrophoresed in 12% bis-Tris gels (Bio-Rad), and the bands were visualized by Coomassie Blue staining. The rest of each sample was also subject to SDS-PAGE and electrotransferred to an ImmobilonP^{SQ} membrane (Millipore, Bedford, MA) for N-terminal sequencing.

qRT-PCR

A 10-ml cell culture in LB grown overnight in the dark at 37 °C was diluted 1:100 with fresh LB and grown in the dark or light for 5 h to an optical density at 600 nm of ~0.8. Cells from 5 ml of this culture were pelleted and stored at −70 °C. These were resuspended in 200 μl of RNase-free lysis buffer (10 mM Tris, pH 8.0, 1 mM EDTA, 10 mM NaCl, 1% SDS) and lysed in a Mini-beadbeater (BioSpec). RNA was purified using the PureLink RNA Minikit (ThermoFisher Scientific) and recommended protocols for TRIzol/chloroform extraction, isopropyl alcohol precipitation, and 70% ethanol wash. This RNA was treated with Turbo DNase I (Ambion), checked in native 1% agarose gels, and quantified in NanoDrop ND-1000 (Thermo Fisher Scientific). RNA (5 μg/20 μl) was reverse transcribed to cDNA with SuperScript IV Reverse Transcriptase (Thermo Fisher Scientific). qRT-PCR was performed in a StepOne instrument (Applied Biosystems) using the 1-Step RT-PCR program cycle for samples containing 1 μl of cDNA, 10 μl of SYBR Green PCR Master Mix (Bio-Rad), and the required primers (400 nM; Table S2), which were designed using the Primer Express 3.0 software to amplify an ~50–150 bp region within each transcript (*sigA* served as the reference gene). A sample with an equivalent volume of RNA served as the control to check the lack of contaminant DNA. Melting and dissociation curves were determined at 60–95 °C, 30 s, and 95 °C, 15 s. Each primer pair was tested for RT-PCR analysis on a standard curve generated from five 10-fold serial dilutions of cDNA. Only primer pairs with efficiency close to 100% were used and data were analyzed using the Applied Biosystems software. Target gene expression is reported relative to the WT level of the gene in the dark as calibrator, as the mean ± S.E. from at least three independent experiments.

In silico modeling and analysis

Details for *in silico* modeling and analysis are provided under Figs. S9 and S11. The systems built were: CarH$_{Tt}$ tetramer in complex with DNA, and with its linker replaced by the longer one from CarH$_{Bm}$; CarH$_{Bm}$ tetramer free or bound to DNA (both homology modeled based on the CarH$_{Tt}$ structures, because our data indicate that CarH$_{Bm}$ has a similar secondary structure and also binds to DNA as a tetramer). AMBER ff14SB (51) was employed to simulate the protein and PARMBSC1 (52) force field parameters to describe DNA. Parameters for base-off His-on AdoCbl were derived consistent with the AMBER ff. All systems were solvated with truncated octahedral boxes of TIP3P (53) waters with a buffer of 12 Å in all directions, and adding K$^+$ ions to neutralization with excess 150 mM KCl. Molecular dynamics (MD) simulations were performed using the AMBER 14 package (54) at constant pressure (1 atm) and temperature (300 K) in 2-fs steps, applying periodic boundary conditions and state-of-the-art simulation protocols. Unrestrained MD simulation (total 500 ns) was performed for each system to study the behavior of the linkers in the context of CarH$_{Tt}$ and CarH$_{Bm}$. For steered MD simulations (36), we built a CarH$_{Tt}$ system bound to DNA with a fourth DNA repeat (DR4) modeled, and a homology model of CarH$_{Bm}$ bound to the same DNA to assess the binding of its DBD to DNA. Genome-wide scan of putative CarH$_{Bm}$ DNA-binding sites was carried out using Artemis (55).

References

1. Elías-Arnanz, M., Padmanabhan, S., and Murillo, F. J. (2011) Light-dependent gene regulation in nonphototrophic bacteria. *Curr. Opin. Microbiol.* **14,** 128 –135 CrossRef Medline

2. Glaeser, J., Nuss, A. M., Berghoff, B. A., and Klug, G. (2011) Singlet oxygen stress in microorganisms. *Adv. Microb. Physiol.* **58,** 141–173 CrossRef Medline

3. Li, Z., Wakao, S., Fischer, B. B., and Niyogi, K. K. (2009) Sensing and responding to excess light. *Annu. Rev. Plant Biol.* **60,** 239 –260 CrossRef Medline

4. Palczewski, K. (2012) Chemistry and biology of vision. *J. Biol. Chem.* **287,** 1612–1619 CrossRef Medline

5. Purcell, E. B., and Crosson, S. (2008) Photoregulation in prokaryotes. *Curr. Opin. Microbiol.* **11,** 168–178 CrossRef Medline

6. Ziegelhoffer, E. C., and Donohue, T. J. (2009) Bacterial responses to photo-oxidative stress. *Nat. Rev. Microbiol.* **7,** 856–863 CrossRef Medline

7. Möglich, A., Yang, X., Ayers, R. A., and Moffat, K. (2010) Structure and function of plant photoreceptors. *Annu. Rev. Plant Biol.* **61,** 21–47 CrossRef Medline

8. Díez, A. I., Ortiz-Guerrero, J. M., Ortega, A., Elías-Arnanz, M., Padmanabhan, S., and García de la Torre, J. (2013) Analytical ultracentrifugation studies of oligomerization and DNA-binding of TtCarH, a *Thermus thermophilus* coenzyme B$_{12}$-based photosensory regulator. *Eur. Biophys. J.* **42,** 463–476 CrossRef Medline

9. Jost, M., Fernández-Zapata, J., Polanco, M. C., Ortiz-Guerrero, J. M., Chen, P. Y., Kang, G., Padmanabhan, S., Elías-Arnanz, M., and Drennan, C. L. (2015) Structural basis for gene regulation by a B$_{12}$-dependent photoreceptor. *Nature* **526,** 536–541 CrossRef Medline

10. Kutta, R. J., Hardman, S. J., Johannissen, L. O., Bellina, B., Messiha, H. L., Ortiz-Guerrero, J. M., Elías-Arnanz, M., Padmanabhan, S., Barran, P., Scrutton, N. S., and Jones, A. R. (2015) The photochemical mechanism of a B$_{12}$-dependent photoreceptor protein. *Nat. Commun.* **6,** 7907 CrossRef Medline

11. Ortiz-Guerrero, J. M., Polanco, M. C., Murillo, F. J., Padmanabhan, S., and Elías-Arnanz, M. (2011) Light-dependent gene regulation by a coenzyme B$_{12}$-based photoreceptor. *Proc. Natl. Acad. Sci. U.S.A.* **108,** 7565–7570 CrossRef Medline

12. Padmanabhan, S., Jost, M., Drennan, C. L., and Elías-Arnanz, M. (2017) A new facet of vitamin B$_{12}$: gene regulation by cobalamin-based photoreceptors. *Annu. Rev. Biochem.* **86,** 485–514 CrossRef Medline

13. Pérez-Marín, M. C., Padmanabhan, S., Polanco, M. C., Murillo, F. J., and Elías-Arnanz, M. (2008) Vitamin B$_{12}$ partners the CarH repressor to downregulate a photoinducible promoter in *Myxococcus xanthus. Mol. Microbiol.* **67,** 804–819 Medline

14. Chatelle, C., Ochoa-Fernandez, R., Engesser, R., Schneider, N., Beyer, H. M., Jones, A. R., Timmer, J., Zurbriggen, M. D., and Weber, W. (2018) A green-light-responsive system for the control of transgene expression in mammalian and plant cells. *ACS Synth. Biol.* **7,** 1349–1358 CrossRef Medline

15. Kainrath, S., Stadler, M., Reichhart, E., Distel, M., and Janovjak, H. (2017) Green-light-induced inactivation of receptor signaling using cobalamin-binding domains. *Angew. Chem. Int. Ed. Engl.* **56,** 4608–4611 CrossRef Medline

16. Wang, R., Yang, Z., Luo, J., Hsing, I. M., and Sun, F. (2017) B$_{12}$-dependent photoresponsive protein hydrogels for controlled stem cell/protein release. *Proc. Natl. Acad. Sci. U.S.A.* **114,** 5912–5917 CrossRef Medline

17. García-Moreno, D., Polanco, M. C., Navarro-Avilés, G., Murillo, F. J., Padmanabhan, S., and Elías-Arnanz, M. (2009) A vitamin B$_{12}$-based system for conditional expression reveals *dksA* to be an essential gene in *Myxococcus xanthus. J. Bacteriol.* **191,** 3108–3119 CrossRef Medline

18. Takano, H., Kondo, M., Usui, N., Usui, T., Ohzeki, H., Yamazaki, R., Washioka, M., Nakamura, A., Hoshino, T., Hakamata, W., Beppu, T., and Ueda, K. (2011) Involvement of CarA/LitR and CRP/FNR family transcriptional regulators in light-induced carotenoid production in *Thermus thermophilus. J. Bacteriol.* **193,** 2451–2459 CrossRef

19. Drennan, C. L., Huang, S., Drummond, J. T., Matthews, R. G., and Lidwig, M. L. (1994) How a protein binds B$_{12}$: a 3.0 Å x-ray structure of B$_{12}$-binding domains of methionine synthase. *Science* **266,** 1669–1674 CrossRef Medline

20. Heldwein, E. E., and Brennan, R. G. (2001) Crystal structure of the transcription activator BmrR bound to DNA and a drug. *Nature* **409,** 378–382 CrossRef Medline

21. Newberry, K. J., and Brennan, R. G. (2004) The structural mechanism for transcription activation by MerR family member multidrug transporter activation, N terminus. *J. Biol. Chem.* **279,** 20356–20362 CrossRef Medline

22. Philips, S. J., Canalizo-Hernandez, M., Yildirim, I., Schatz, G. C., Mondragón, A., and O'Halloran, T. V. (2015) Allosteric transcriptional regulation via changes in the overall topology of the core promoter. *Science* **349,** 877–881 CrossRef Medline

23. Watanabe, S., Kita, A., Kobayashi, K., and Miki, K. (2008) Crystal structure of the [2Fe-2S] oxidative-stress sensor SoxR bound to DNA. *Proc. Natl. Acad. Sci. U.S.A.* **105,** 4121–4126 CrossRef Medline

24. Jost, M., Simpson, J. H., and Drennan, C. L. (2015) The transcription factor CarH safeguards use of adenosylcobalamin as a light sensor by altering the photolysis products. *Biochemistry* **54,** 3231–3234 CrossRef Medline

25. Takano, H., Mise, K., Hagiwara, K., Hirata, N., Watanabe, S., Toriyabe, M., Shiratori-Takano, H., and Ueda, K. (2015) Role and function of LitR, an adenosyl B$_{12}$-bound light-sensitive regulator of *Bacillus megaterium* QM B1551, in regulation of carotenoid production. *J. Bacteriol.* **197,** 2301–2315 CrossRef Medline

26. Newberry, K. J., Nakano, S., Zuber, P., and Brennan, R. G. (2005) Crystal structure of the *Bacillus subtilis* anti-α, global transcriptional regulator, Spx, in complex with the α C-terminal domain of RNA polymerase. *Proc. Natl. Acad. Sci. U.S.A.* **102,** 15839–15844 CrossRef Medline

27. Zuber, P. (2009) Management of oxidative stress in *Bacillus. Annu. Rev. Microbiol.* **63,** 575–597 CrossRef Medline

28. Schmid, F. X. (1997) Optical spectroscopy to characterize protein conformation and conformational changes. in *Protein structure: a practical approach* (Creighton, T. E., ed) pp. 261–297, Oxford University Press, Oxford, UK

29. Rohl, C. A., and Baldwin, R. L. (1997) Comparison of NH exchange and circular dichroism as techniques for measuring the parameters of the helix-coil transition in peptides. *Biochemistry* **36,** 8435–8442 CrossRef Medline

30. Baldwin, R. L., and Rose, G. D. (2013) Molten globules, entropy-driven conformational change and protein folding. *Curr. Opin. Struct. Biol.* **23,** 4–10 CrossRef Medline

31. Goto, Y., and Fink, A. L. (1989) Conformational states of beta-lactamase: molten-globule states at acidic and alkaline pH with high salt. *Biochemistry* **28,** 945–952 CrossRef Medline

32. Semisotnov, G. V., Rodionova, N. A., Razgulyaev, O. I., Uversky, V. N., Gripas, A. F., and Gilmanshin, R. I. (1991) Study of the "molten globule" intermediate state in protein folding by a hydrophobic fluorescent probe. *Biopolymers* **31,** 119–128 CrossRef Medline

33. Iniesta, A. A., García-Heras, F., Abellón-Ruiz, J., Gallego-García, A., and Elías-Arnanz, M. (2012) Two systems for conditional gene expression in *Myxococcus xanthus* inducible by isopropyl-β-D-thiogalactopyranoside or vanillate. *J. Bacteriol.* **194,** 5875–5885 CrossRef Medline

34. Meiser, P., Bode, H. B., and Müller, R. (2006) The unique DKxanthene secondary metabolite family from the myxobacterium *Myxococcus xanthus* is required for developmental sporulation. *Proc. Natl. Acad. Sci. U.S.A.* **103,** 19128–19133 CrossRef Medline

35. Craig, M. L., Suh, W. C., and Record, M. T., Jr. (1995) HO⋅ and DNase I probing of Eσ^{70} RNA polymerase- λP$_R$ promoter open complexes: Mg^{2+} binding and its structural consequences at the transcription start site. *Biochemistry* **34,** 15624–15632 CrossRef Medline

36. Grubmüller, H., Heymann, B., and Tavan, P. (1996) Ligand binding: molecular mechanics calculation of the streptavidin-biotin rupture force. *Science* **271,** 997–999 CrossRef Medline

37. Birukou, I., Seo, S. M., Schindler, B. D., Kaatz, G. W., and Brennan, R. G. (2014) Structural mechanism of transcription regulation of the *Staphylococcus aureus* multidrug efflux operon *mepRA* by the MarR family repressor MepR. *Nucleic Acids Res.* **42,** 2774–2788 CrossRef Medline

38. Fuxreiter, M., Simon, I., and Bondos, S. (2011) Dynamic protein-DNA recognition: beyond what can be seen. *Trends Biochem. Sci.* **36,** 415–423 CrossRef Medline

39. Vuzman, D., and Levy, Y. (2012) Intrinsically disordered regions as affinity tuners in protein-DNA interactions. *Mol. Biosyst.* **8,** 47–57 CrossRef Medline

40. Motlagh, H. N., Wrabl, J. O., Li, J., and Hilser, V. J. (2014) The ensemble nature of allostery. *Nature* **508,** 331–339 CrossRef Medline

41. Gao, Y., Foo, Y. H., Winardhi, R. S., Tang, Q., Yan, J., and Kenney, L. J. (2017) Charged residues in the H-NS linker drive DNA binding and gene silencing in single cells. *Proc. Natl. Acad. Sci. U.S.A.* **114,** 12560–12565 CrossRef Medline

≋ASBMB

42. van Leeuwen, H. C., Strating, M. J., Rensen, M., de Laat, W., and van der Vliet, P. C. (1997) Linker length and composition influence the flexibility of Oct-1 DNA binding. *EMBO J.* **16,** 2043–2053 CrossRef Medline

43. Vuzman, D., Polonsky, M., and Levy, Y. (2010) Facilitated DNA search by multidomain transcription factors: cross talk via a flexible linker. *Biophys. J.* **99,** 1202–1211 CrossRef Medline

44. Flock, T., Weatheritt, R. J., Latysheva, N. S., and Babu, M. M. (2014) Controlling entropy to tune the functions of intrinsically disordered regions. *Curr. Opin. Struct. Biol.* **26,** 62–72 CrossRef Medline

45. Barendt, S., Lee, H., Birch, C., Nakano, M. M., Jones, M., and Zuber, P. (2013) Transcriptomic and phenotypic analysis of paralogous *spx* gene function in *Bacillus anthracis* Sterne. *Microbiologyopen* **2,** 695–714 CrossRef Medline

46. Park, D. M., and Kiley, P. J. (2014) The influence of repressor DNA binding site architecture on transcriptional control. *mBio* **5,** e01684-01614 Medline

47. Weber, G., and Young, L. B. (1964) Fragmentation of bovine serum albumin by pepsin: I. the origin of the acid expansion of the albumin molecule. *J. Biol. Chem.* **239,** 1415–1423 Medline

48. Wittchen, K. D., and Meinhardt, F. (1995) Inactivation of the major extracellular protease from *Bacillus megaterium* DSM319 by gene replacement. *Appl. Microbiol. Biotechnol.* **42,** 871–877 CrossRef Medline

49. Biedendieck, R., Borgmeier, C., Bunk, B., Stammen, S., Scherling, C., Meinhardt, F., Wittmann, C., and Jahn, D. (2011) Systems biology of recombinant protein production using *Bacillus megaterium*. *Methods Enzymol.* **500,** 165–195 CrossRef Medline

50. Gallego-García, A., Iniesta, A. A., González, D., Collier, J., Padmanabhan, S., and Elías-Arnanz, M. (2017) *Caulobacter crescentus* CdnL is a nonessential RNA polymerase-binding protein whose depletion impairs normal growth and rRNA transcription. *Sci. Rep.* **7,** 43240 CrossRef Medline

51. Maier, J. A., Martinez, C., Kasavajhala, K., Wickstrom, L., Hauser, K. E., and Simmerling, C. (2015) ff14SB: improving the accuracy of protein side chain and backbone parameters from ff99SB. *J. Chem. Theory Comput.* **11,** 3696–3713 CrossRef Medline

52. Ivani, I., Dans, P. D., Noy, A., Pérez, A., Faustino, I., Hospital, A., Walther, J., Andrio, P., Goñi, R., Balaceanu, A., Portella, G., Battistini, F., Gelpí, J. L., González, C., Vendruscolo, M., *et al.* (2016) Parmbsc1: a refined force field for DNA simulations. *Nat. Methods* **13,** 55–58 CrossRef Medline

53. Jorgensen, W. L., Chandrasekhar, J., Madura, J. D., Impey, R. W., and Klein, M. L. (1983) Comparison of simple potential functions for simulating liquid water. *J. Chem. Phys.* **79,** 926–935 CrossRef

54. Case, D. A., Babin, V., Berryman, J. T., Betz, R. M., Cai, Q., Cerutti, D. S., Cheatham, T. E., Darden, T. A., Duke, R. E., Gohlke, H., Goetz, A. W., Gusarov, S., Homeyer, N., Janowski, P., Kaus, J., *et al.* (2014) *Amber* 14, University of California, San Francisco, CA

55. Rutherford, K., Parkhill, J., Crook, J., Horsnell, T., Rice, P., Rajandream, M. A., and Barrell, B. (2000) Artemis: sequence visualization and annotation. *Bioinformatics* **16,** 944–945 CrossRef Medline

ASBMB

J. Biol. Chem. (2018) 293(46) 17888–17905 **17905**

Plasticity in oligomerization, operator architecture, and DNA binding in the mode of action of a bacterial B $_{12}$-based photoreceptor

Jesús Fernández-Zapata, Ricardo Pérez-Castaño, Juan Aranda, Francesco Colizzi, María Carmen Polanco, Modesto Orozco, S. Padmanabhan and Montserrat Elías-Arnanz

Access the most updated version of this article at doi: 10.1074/jbc.RA118.004838

Alerts:
- When this article is cited
- When a correction for this article is posted

Click here to choose from all of JBC's e-mail alerts

This article cites 53 references, 17 of which can be accessed free at
http://www.jbc.org/content/293/46/17888.full.html#ref-list-1